REPORT DOCUMENTATION PAGE

Public Reporting burden for this collection of information is estimated to average 1 hour per response, including the time for reviewing instructions, searching existing data sources, gathering and maintaining the data needed, and completing and reviewing the collection of information. Send comment regarding this burden estimates or any other aspect of this collection of information, including suggestions for reducing this burden, to Washington Headquarters Services, Directorate for information Operations and Reports, 1215 Jefferson Davis Highway, Suite 1204, Arlington, VA 22202-4302, and to the Office of Management and Budget, Paperwork Reduction Project (0704-0188,) Washington, DC 20503.

1. AGENCY USE ONLY (Leave Blank)	2. REPORT DATE May 29, 2008	3. REPORT TYPE AND DATES COVERED Final report for period 3/1/05 through 2/29/08

4. TITLE AND SUBTITLE

Mathematical Fluid Dynamics of Store and Stage Separation, Multi-Body Flows and Flow Control

5. FUNDING NUMBERS

6. AUTHOR(S)

Norman D. Malmuth and Alexander V. Fedorov

7. PERFORMING ORGANIZATION NAME(S) AND ADDRESS(ES)

Teledyne Scientific & Imaging, 1049 Camino Dos Rios, Thousand Oaks, CA 91360

8. PERFORMING ORGANIZATION REPORT NUMBER

9. SPONSORING / MONITORING AGENCY NAME(S) AND ADDRESS(ES)

Air Force Office of Scientific Research
875 North Randolph Street
Arlington VA 22203-1768

10. SPONSORING / MONITORING AGENCY REPORT NUMBER

11. SUPPLEMENTARY NOTES

The views, opinions and/or findings contained in this report are those of the author(s) and should not be construed as an official Department of the Army position, policy or decision, unless so designated by other documentation.

12 a. DISTRIBUTION / AVAILABILITY STATEMENT

Approved for public release; distribution unlimited.

12 b. DISTRIBUTION CODE

13. ABSTRACT

New insights have been gained in atmospheric and space launch stage separation from our studies of the aerodynamic interference between multiple bodies in supersonic flow. Quick means of estimating and controlling repulsion or attraction lift associated with this interaction is an important enabling technology to size launch separation rocket motors to achieve the best compromise between motor weight and safe staging. In this connection, motor weight reduces usable payload. Asymptotic methods, scattering, slender body theories and CFD modeling have provided valuable systematic approximations schemes that advantageously couple with modern computational methods. Our theoretical solutions for lift force interference between multiple bodies give good agreement with numerical solutions and experimental data. These solutions shed light on important scattering phenomena not previously recognized as relevant to this problem. The analyses allow us to identify lumped dimensionless parameters and provide scaling laws as well as closed-form expressions for the interference not accessible solely from computation that can be used for interpolation and extrapolation of CFD solutions as well as efficient testing and design of new flight vehicles. This approach dramatically simplifies trajectory predictions in which inertial and aerodynamic forces are strongly coupled. The aforementioned modeling has been carried out in the framework of the quasi-steady approximation. However, there are cases when acceleration of the body C.G. and/or the pitching angular velocity are not small and the unsteady effects become appreciable. First steps in mathematical modeling of these effects have been made with emphasis on the body wave drag. Namely, theoretical analysis of the wave drag generated by a non-lifting slender body of revolution during its instantaneous supersonic start was carried out. Typical phases of the transient process were identified. For each phase, analytical solutions of the flow potential and wave drag were obtained. The transient process was also simulated numerically by solving 3-D Euler equations. The theoretical wave drag is in excellent agreement with CFD in all phases of the transient process. These results provide a good launching pad for theoretical modeling of unsteady body motions including the coupling between body dynamics and aerodynamics.

14. SUBJECT TERMS

Store and stage separation, multi-body interference, shock-body interaction, slender body aerodynamics, supersonic flow, asymptotic methods, theory of scattering, wave drag, unsteady aerodynamics

15. NUMBER OF PAGES

16. PRICE CODE

17. SECURITY CLASSIFICATION OR REPORT **UNCLASSIFIED**	18. SECURITY CLASSIFICATION ON THIS PAGE **UNCLASSIFIED**	19. SECURITY CLASSIFICATION OF ABSTRACT **UNCLASSIFIED**	20. LIMITATION OF ABSTRACT UL

Dedicated to memory of Dr. Norman Malmuth

Mathematical Fluid Dynamics of Store and Stage Separation, Multi-Body Flows and Flow Control

Final Report

on AFOSR Contract FA9550-05-C-0030
for the period 3/1/05 through 2/29/08

Prepared by:

Norman D. Malmuth

Teledyne Scientific & Imaging Company
Thousand Oaks, CA 91360

and

Alexander V. Fedorov

Department of Aeromechanics and Flight Engineering
Moscow Institute of Physics and Technology
Zhukovsky, Moscow Region 140180

February 2008

Executive summary

New insights have been gained in atmospheric and space launch stage separation from our studies of the aerodynamic interference between multiple bodies in supersonic flow. Quick means of estimating and controlling repulsion or attraction lift associated with this interaction is an important enabling technology to size launch separation rocket motors to achieve the best compromise between motor weight and safe staging. In this connection, motor weight reduces usable payload.

Asymptotic methods, scattering, slender body theories and CFD modeling have provided valuable systematic approximations schemes that advantageously couple with modern computational methods. Our theoretical solutions for lift force interference between multiple bodies give good agreement with numerical solutions and experimental data. These solutions shed light on important scattering phenomena not previously recognized as relevant to this problem. The analyses allow us to identify lumped nondimensional parameters and provide scaling laws as well as closed-form expressions for the interference not accessible solely from computation that can be used for interpolation and extrapolation of CFD solutions as well as efficient testing and design of new flight vehicles. This approach dramatically simplifies trajectory predictions in which inertial and aerodynamic forces are strongly coupled.

The aforementioned modeling has been carried out in the framework of the quasi-steady approximation. However, there are cases when acceleration of the body C.G. and/or the pitching angular velocity are not small and the unsteady effects become appreciable. First steps in mathematical modeling of these effects have been made with emphasis on the body wave drag. Namely, we have conducted theoretical analysis of the wave drag generated by a non-lifting slender body of revolution during its instantaneous supersonic start. The analysis is based on linear acoustic theory and asymptotic techniques. Typical phases of the transient process were identified. For each phase, analytical expressions of the flow potential and wave drag were derived. A composite solution for the wave-drag coefficient that is uniformly valid throughout the transient process was obtained. The analytical solutions were plugged into a FORTRAN code providing quick calculations of the wave drag versus time. Numerical examples were generated for a slender body of half-sine shape for different Mach numbers of instantaneous body start. It was shown that the initial wave-drag coefficient is significantly larger than its asymptotic level relevant to steady flight. The transient time period increases and tends to infinity as the Mach number decreases and approaches $M = 1$ (transonic case). The transient process was also simulated numerically by solving 3-D Euler equations for Mach=2 start of the aforementioned body. It was shown that the theoretical wave drag is in excellent agreement with CFD in all phases of the transient process. These results provide a good launching pad for theoretical modeling of unsteady body motions including the coupling between body dynamics and aerodynamics.

Our experience in low-order modeling of store separation helped Dr. Malmuth to develop a physics-based predictive tool for quick estimates of the body trajectory in the case of separation from a rectangular cavity to supersonic outer flow. This tool has been used for parametric studies of store trajectories relevant to the HIFEX sled tests. The theoretical predictions along with CFD studies of Boeing convinced the Air Force that the HIFEX store release was not a high-risk event.

1

Persons contributed to the project

N. Malmuth (Teledyne Sientific) – former PI of this project, passed away on July 3, 2007

A. Fedorov (MIPT, Moscow) – Theoretical analyses

V. Soudakov (MIPT, Moscow) – Numerical simulations

O. Ryzhov (University of California) – Technical discussions

H. Hornung (Caltech) – Technical discussions

Table of contents

1. Introduction

Emphasis on safe, high-accuracy, reliable parasite body separation will be critical for parasite body system upgrades to cost-effectively for new aircraft development for the foreseeable future. Although the problem of parasite bodies release from an aircraft platform has received much attention as exemplified by Refs. [1-3], more effort is needed to understand the underlying basic physics and essential parameters. In a larger sense, this technology is a subset of the problem of the interactions between moving bodies in all speed ranges. Multi-body interaction applications include separation and carriage of various stage vehicles for space missions and flight-testing as well as crew escape. For this group, hypersonic multistage vehicle concepts of interest to the U.S. Air Force frequently utilize the launch of a small rocket-powered stage from a large subsonic or transonic aircraft such as the B-52. Other examples are the PEGASUS series and the Shuttle. Currently, multistage launch scenarios are envisioned for future hypersonic and space applications. A new thrust involves the use of air breathing (scramjet or turbo-scramjet) rather than rocket-powered stages. These can be associated with recoverable launch vehicles such as the RLV series (second and third generation) being studied in the Boeing CRI program. Other applications include the Boeing Delta IV series.

The payload mass fraction can be drastically affected by sizing of the separation motors. Overly conservative estimates requiring extra thrust will give a larger weight penalty associated with more motor thrust for stage separation. A smaller (optimistic) separation motor design solution will increase payload with the risk of re-contact and reduced safety. The correctness of these decisions depends on our understanding of the interaction of the fluid dynamics with the dynamics of the motion.

Rather than emphasizing speed, efficiency and accuracy of production CFD codes, we stress computationally non-intense PC application to understand and harness (through new flow control concepts) the important physical mechanisms that pervade a wide class of parasite body and stage separation phenomena. Another emphasis is to formulate representative unit problems and identify new interesting mathematical techniques to solve these problems and combine with them current large-scale numerical techniques. On the other hand, more realism is being introduced as our effort progresses.

Besides the research thrust of stage separation embodied in the effort discussed herein, another is a tie-in with current efforts regarding optimizing parasite bodies-bay acoustic mitigation measures with stage trajectory characteristics, (see [4]). Current control measures include alternate jet blowing and actuators to reduce the amplitudes of the noise power from parasite bodies-bay cavities. Flight and ground tests are underway to investigate the effects on parasite body trajectories. The physics and time scales of the mitigation measures and their possible coupling with the dynamic characteristics of the separation bodies needs to be better understood. Our models provide useful insight into this interaction. Examples of our work are in Refs. [5-16].

2. Major accomplishments

A major thrust in FY 2005-2006 was a mathematical modeling of lift and pitching moment associated with the two-body interaction. The general mathematical ideas were discussed in [16] and key unit problems are shown in Figure 1. Special emphasis was on Problems 1, 2 and 4 relevant to scattering of the parent-body-induced shock wave by the parasite body.

4

In FY 2005 we studied the interaction between the wedge-induced shock and a cylinder using the theory of scattering (Problem 1) [15]. The lift force associated with multi-scattering of the wing-induced shock wave by a slender body of revolution was analyzed using linearized supersonic theory, scattering theory [17,18] and asymptotic methods [19-21]. Although acoustical and electromagnetic analyses such as those just cited are well known, their application to supersonic shock-wave scattering problems has not received significant attention.The local and integral lift coefficients were obtained in simple analytical forms convenient for quick calculations of the aerodynamic loads. These solutions can be applied to the moderate supersonic (Mach numbers from 1.2 to 3) multi-body interaction problem for crosscheck with other computational or engineering methods.


Problem 1: Plane shock-parasite body interaction

Problem 2: parasite body-induced wave train

Problem 3: parasite body-induced wave-train including expansion waves

Problem 4: Two body interaction

Problem 5: Wave train between two wedges
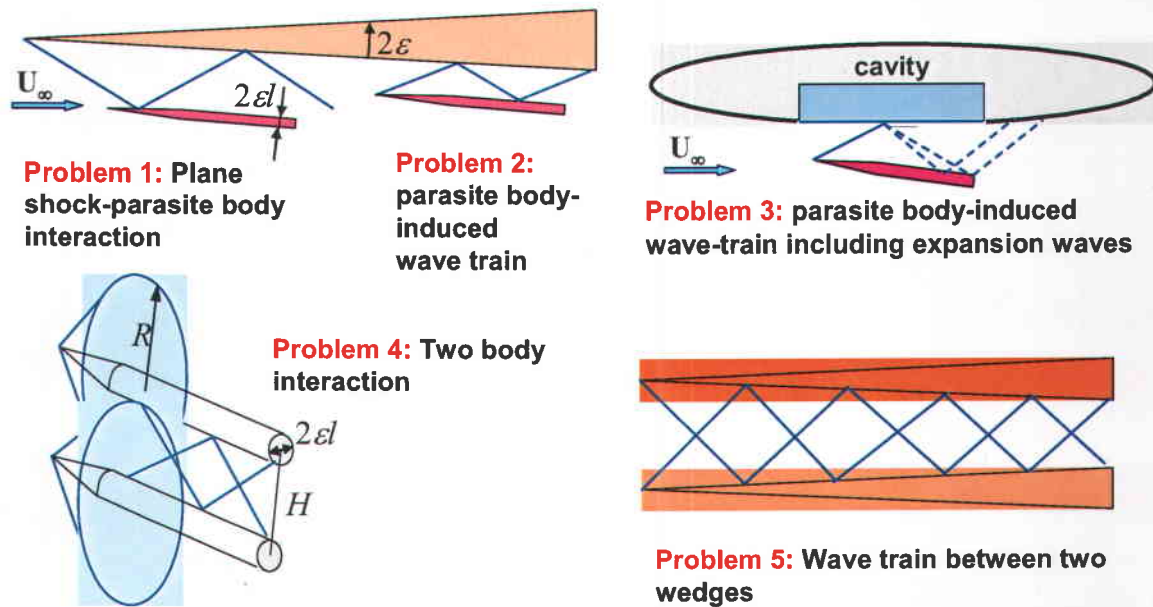
Figure 1 Unit problems relevant to supersonic stage separation.

The local analytical solution, which provides detailed distribution of the lift-force coefficient on the length scale ~ body radius, is shown by the black line in Figure 2. The global solution ignores local details and gives the step-function distribution shown by the red line. It was found that the total lift is predominantly generated by the first scattering. We conduced series of Euler CFD calculations for Mach=2 free stream (Figure 3), and showed that the total lift-force coefficient predicted by CFD (red symbols) agrees well with the theoretical solution (black line). The analytical solution, which is inaccessible from purely numerical methods, shows the excellent complementarity of the numerics and the pen-and-paper methods. On the other, the numerics shows accessibility to nonlinear effects not modeled by the linear theory.

We also showed that the analytical solution agrees satisfactory with the experimental data [22] (Figures 4 and 5) obtained for the blunt-base parabolic body of revolution in the flow-field induced by a circular-arc wing in the Mach=2 free stream, despite the fact that the body radius varies in the interaction region and the wing thickness is not very small (the wing thickness ratio is 1/6). This adds more confidence in practicability of the theoretical model [15].
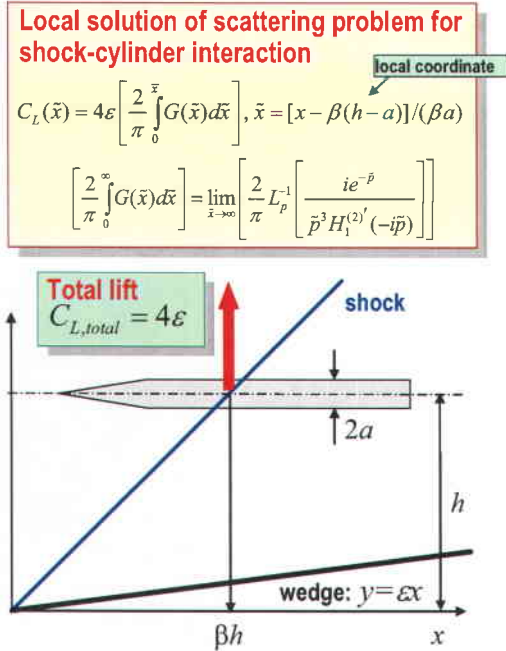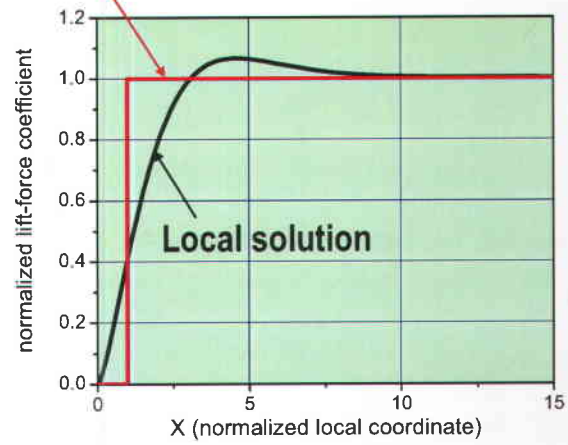
Figure 2 Lift force C_L induced by scattering of the parent-body-induced shock wave by the parasite body.
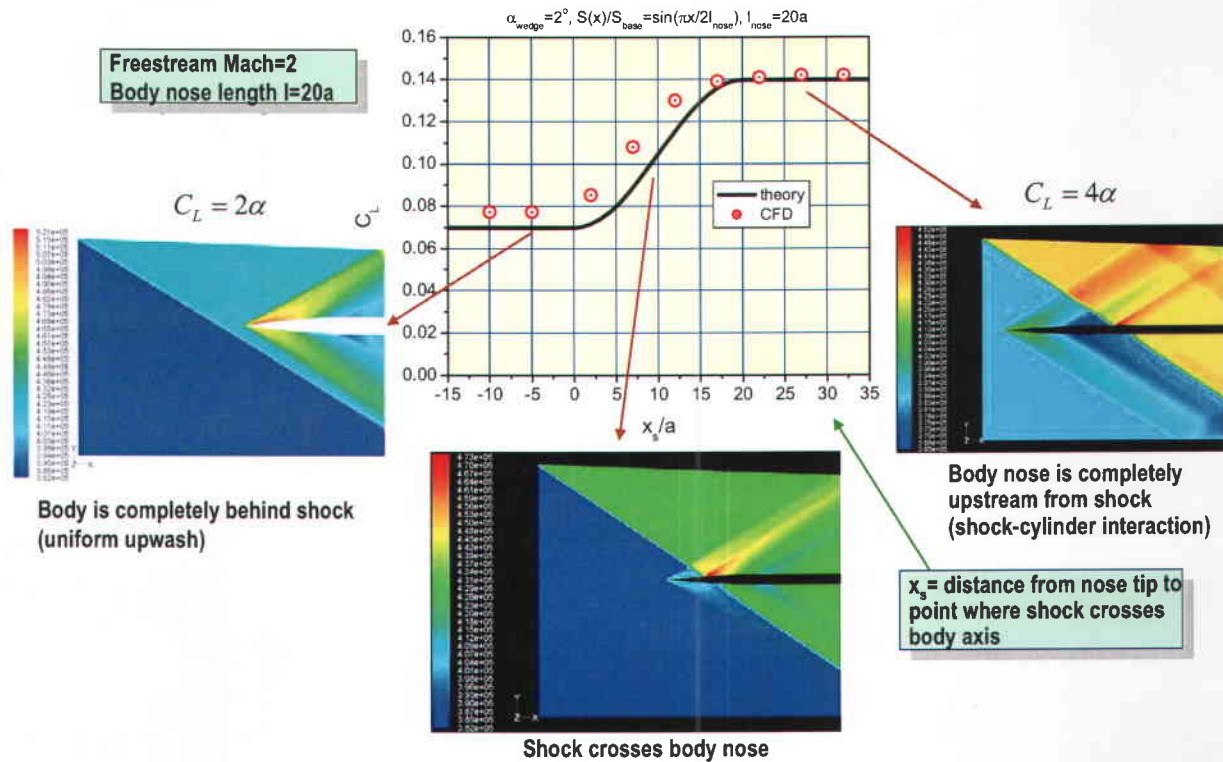

Figure 3 The total lift force predicted by theory (black line) agrees well with the Euler CFD solution (symbols and panels showing the pressure field).
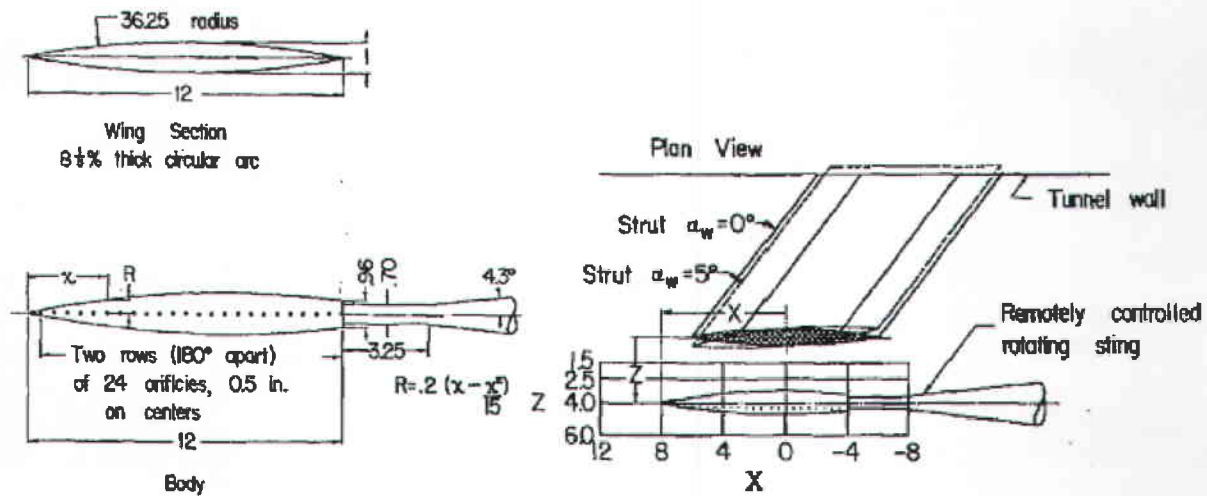
Figure 4 Schematic layout of test setup and models (scanned from Figure 1 of Ref. [22]).
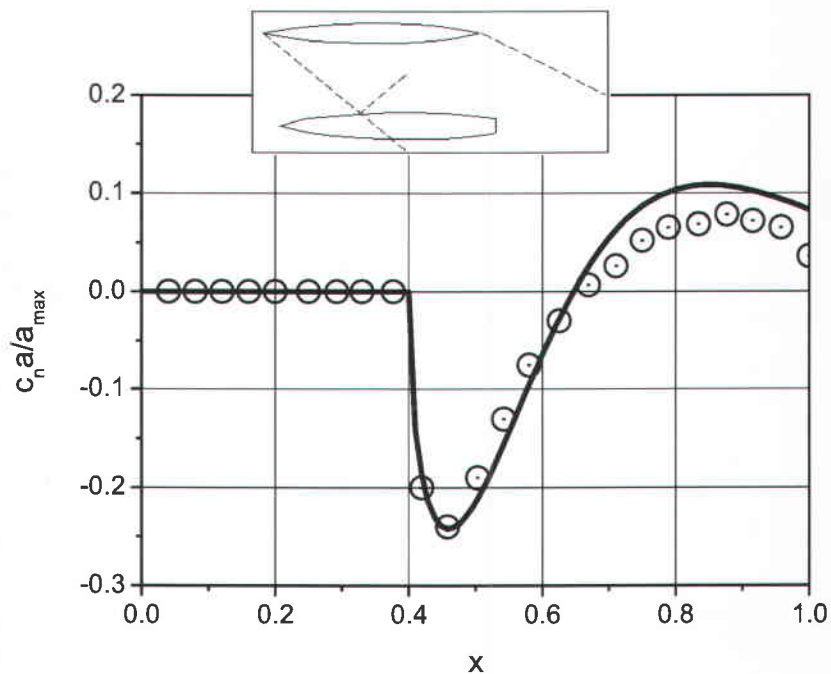

Figure 5 Comparison of theoretical (solid line) and experimental (symbols) distributions of the normal force induced by the wing shock impinging on the body at $x \approx 0.4$.

In FY 2006, we treated the case of two-body interference schematically shown in Figure 6 [23]. For this configuration, the cross sectional shape of both bodies is a function of the axial coordinate, and bodies generate 3-D flow disturbances with appreciable streamwise variations over the body length.
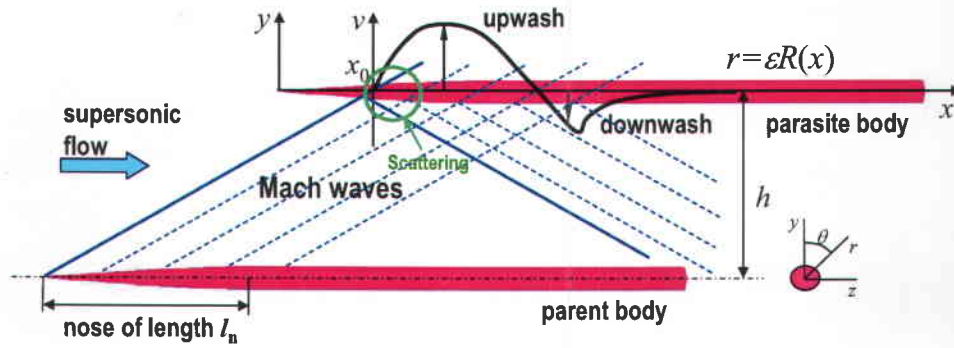
Flow potential: $\Phi(x,y,z;M_\infty,\varepsilon) \equiv \dfrac{\Phi^*}{U_\infty^* L^*} = x + \phi(x,y,z;\beta,\varepsilon) + ..., \quad \beta \equiv \sqrt{M^2 - 1}$

3-D problem: $\beta^2 \partial_x^2 \phi - \left(\partial_y^2 \phi + \partial_z^2 \phi\right) = 0$

$\partial_n \phi = 0$ **on parent-body surface**

$\partial_n \phi = 0$ **on parasite-body surface**

Figure 6 Problem of the two-body interaction.

The problem is analyzed using two essentially different approaches:

- Approach 1 provides a global solution. The problem is solved using asymptotic methods as well as the basic idea of slender body theory – replace bodies by distributions of sources and doublets

- Approach 2 is based on the shock-wave scattering theory. In this connection, the theoretical model [15] developed in 2005 was extended to the case of two bodies of revolution

These two approaches complement each other: the first provides a global structure of the lift force distribution, the second provides flow details in local regions associated with rapid changes of incoming (parent-body-induced) flow field in the vicinity of the parasite body such as shock-body interaction regions.

We started with Approach 1 and considered a parasite body in the parent-body-induced nonuniform supersonic flow (Figure 7). For large vertical distance between bodies ($h/a \sim \varepsilon^{-1}$), the parent-body-induced disturbance is predominantly two-dimensional (to relative accuracy $O(\varepsilon^2)$) in the vicinity of parasite body. This potential gives the vertical velocity on the parasite body axis (see the first box). The vertical velocity perturbation is treated as the induced angle of attack. The parasite body is replaced by line-distributions of sources and doublets. In the vicinity of parasite body axis, the radial velocity (induced by parasite body) has the form shown in the second box. From boundary conditions on the parasite body surface we obtain intensities of sources and doublets (see the third box). Then we calculate the pressure coefficient on the

8

parasite body surface and extract its asymmetric part, which contributes to the lift force (see the fourth box). Integrating the asymmetric part of pressure coefficient over the parasite body surface, we obtain the axial distribution of the lift-force coefficient (see the pink box).
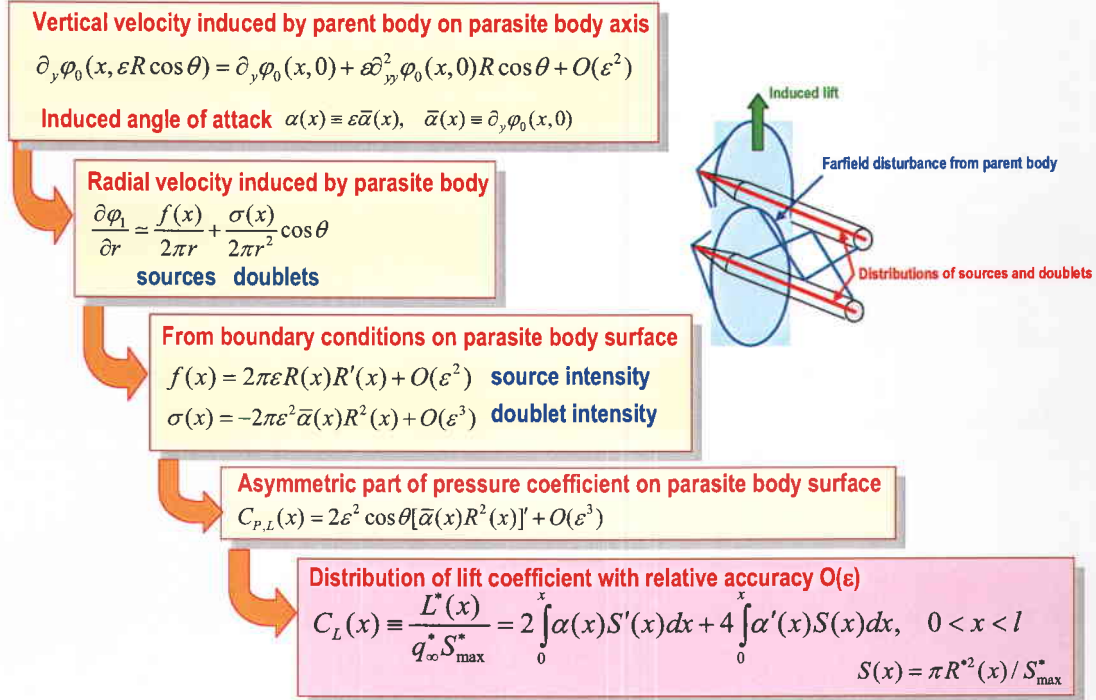

Vertical velocity induced by parent body on parasite body axis

$$\partial_y \varphi_0(x, \varepsilon R \cos\theta) = \partial_y \varphi_0(x,0) + \varepsilon \partial^2_{yy} \varphi_0(x,0) R \cos\theta + O(\varepsilon^2)$$

Induced angle of attack $\alpha(x) \equiv \varepsilon \bar{\alpha}(x), \quad \bar{\alpha}(x) \equiv \partial_y \varphi_0(x,0)$

Radial velocity induced by parasite body

$$\frac{\partial \varphi_1}{\partial r} \simeq \frac{f(x)}{2\pi r} + \frac{\sigma(x)}{2\pi r^2} \cos\theta$$

sources   doublets

From boundary conditions on parasite body surface

$$f(x) = 2\pi\varepsilon R(x)R'(x) + O(\varepsilon^2) \quad \text{source intensity}$$
$$\sigma(x) = -2\pi\varepsilon^2 \bar{\alpha}(x)R^2(x) + O(\varepsilon^3) \quad \text{doublet intensity}$$

Asymmetric part of pressure coefficient on parasite body surface
$$C_{P,L}(x) = 2\varepsilon^2 \cos\theta [\bar{\alpha}(x)R^2(x)]' + O(\varepsilon^3)$$

Distribution of lift coefficient with relative accuracy O(ε)
$$C_L(x) \equiv \frac{L^*(x)}{q^*_\infty S^*_{max}} = 2\int_0^x \alpha(x)S'(x)dx + 4\int_0^x \alpha'(x)S(x)dx, \quad 0 < x < l$$
$$S(x) = \pi R^{*2}(x)/S^*_{max}$$

Induced lift

Farfield disturbance from parent body

Distributions of sources and doublets

Figure 7 Major steps of Approach 1 providing the global solution.

To illustrate basic features of the two-body interaction we analyzed the interaction between two identical bodies, which have a sine-shaped nose of length l_n and a long cylindrical afterbody. The vertical distance between bodies was fixed, $h = l_n$, whereas the streamwise distance between the nose tips was variable. Figure 8 shows the normalized lift-force coefficient as a function of x_0 – streamwise distance from the parasite body tip to the point where the parent-body-induced shock crosses the parasite-body axis.

The yellow frame in Figure 8 indicates the case, when the parent-induced disturbance interacts with the cylindrical afterbody only. This case has been studied in details using Approach 2 based on the scattering theory. Basic steps of this analysis are shown in Figure 9. The analysis is started with replacing of the parent body by the line-source distribution. The Laplace transform of corresponding perturbation potential contains modified Bessel function K_0 (see the first box). Asymptotic expansion of this transform for large argument gives a solution, which can be treated as a plane wave radiating the parasite-body cylindrical surface. The interaction of each plain wave with the cylinder is solved analytically using methods of the scattering theory. Solution of this unit problem provides the pressure distribution on the parasite body. Integrating this pressure over the parasite body surface we obtain Fourier components of the local lift coefficient from each elementary wave (see the second box). The inverse Laplace transform gives the local lift

coefficient per unit length (see the third box). Finally, we obtain the axial distribution of lift-force coefficient shown in the pink box.
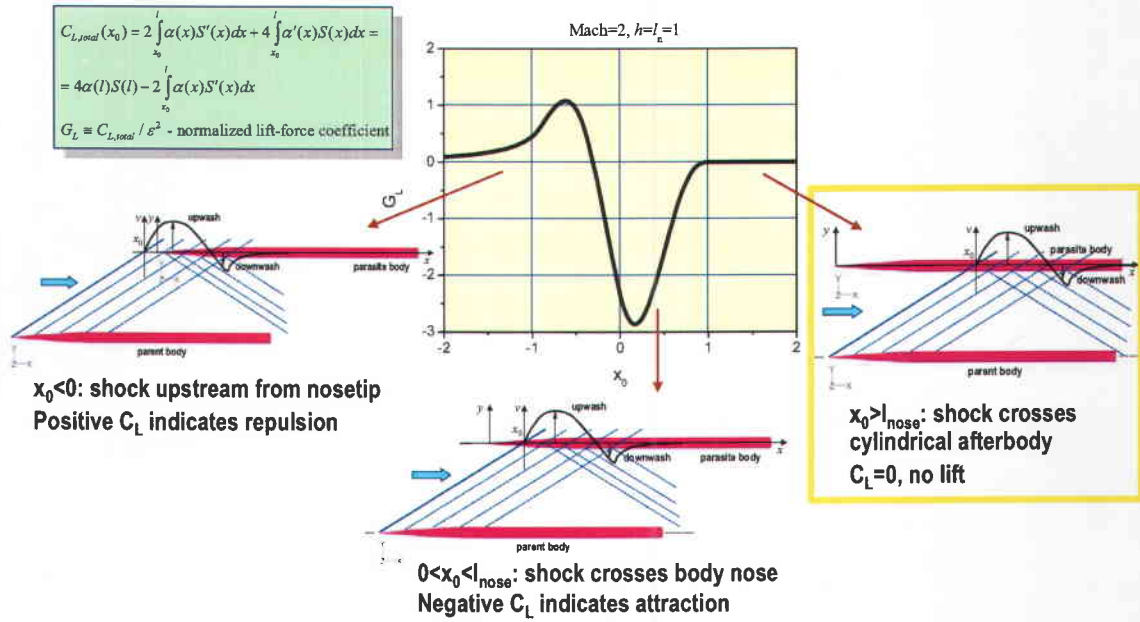

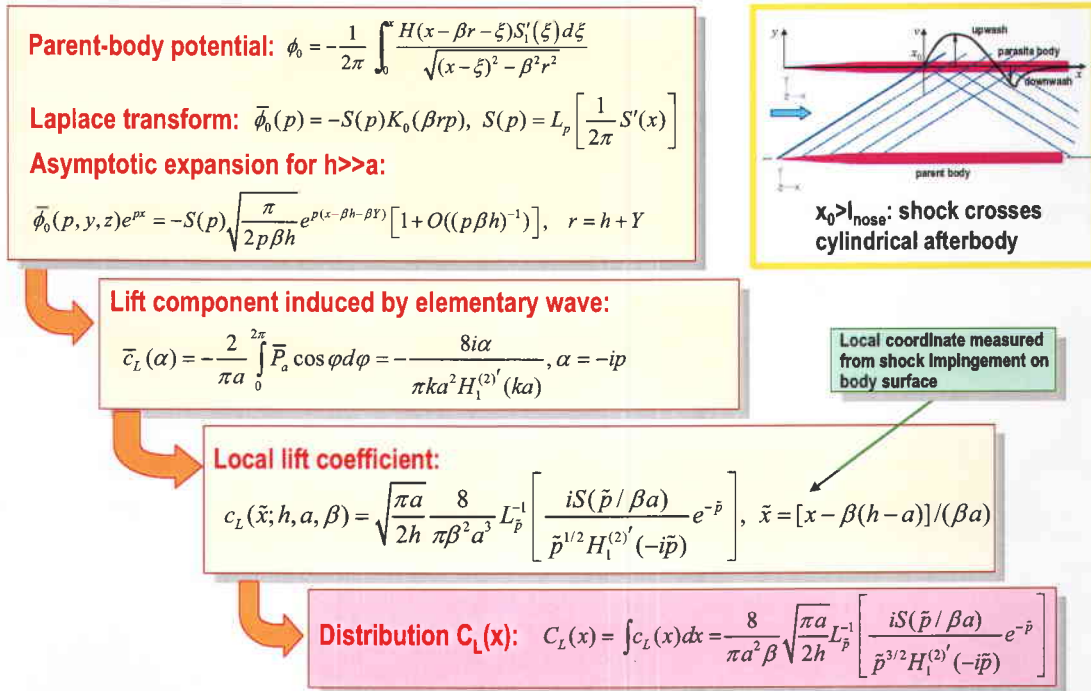**Figure 8** Lift due to the interaction between two identical bodies of revolution (Approach 1).

Figure 9 Basic steps in solving the scattering problem for the shock scattering on the cylindrical afterbody (Approach 2).

10

To verify aforementioned theoretical models, we carried out 3-D Euler simulation of this problem (Figure 10). For two identical bodies with aligned nosetips, the problem is identical to that for one body over a horizontal plane at the vertical distance $h/2$ from the body axis. The computational domain for this configuration is shown in the left bottom corner. The pressure, temperature and Mach number distributions in the symmetry plane as well as the pressure distribution on the body surface indicate a complex structure of induced and reflected disturbances.
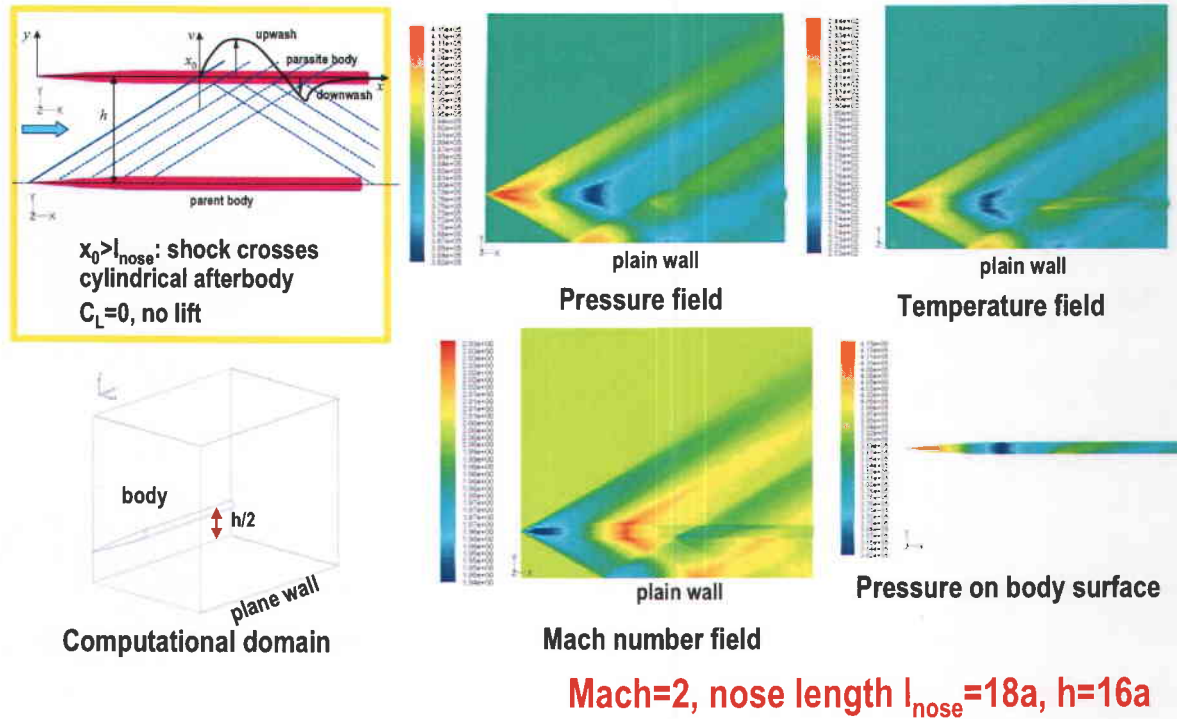
Figure 10 3-D Euler CFD solution for two identical slender bodies of revolution.

Figure 11 compares the theoretical distributions of $C_L(x)$ with the CFD solution. The blue line shows the global solution obtained with Approach 1 (see Figure 7). The black line corresponds to the local solution obtained with Approach 2 based on the scattering problem (see Figure 9). The red symbols show the Euler CFD data. Despite 3-D complexity of two-body interference, the leading-order analytical solutions agree with the CFD to $O(\varepsilon)$.

We also considered the scaling issue of the two-body interaction (Figure 12). The analytical forms of global and local asymptotic solutions allowed us to formulate the scaling law (see the pink box). Robustness of this scaling was estimated using parametric calculations of the lift-force coefficient as a function of x_0 (streamwise distance from the nose tip to the point where the shock crosses the body axis) at various vertical distances between two identical bodies (see the left plot) and various Mach numbers (the right plot). It is seen that these dependencies quickly collapse to a universal curve as the separation distance h and/or the freestream Mach number increases. Using this scaling it is feasible to interpolate/extrapolate CFD solutions and dramatically reduce the computational effort that is of critical importance for quick assessments of aerodynamic coefficients at various time moments during the separation process.
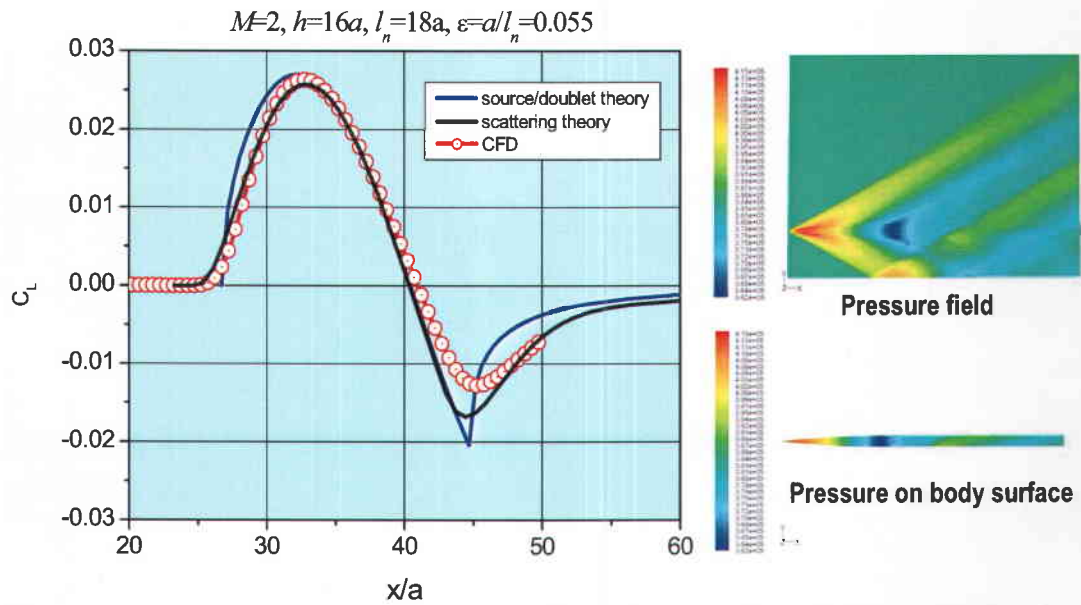
11

Figure 11 Comparison of theoretical and CFD solution for the lift force coefficient distribution along the parasite body axis.
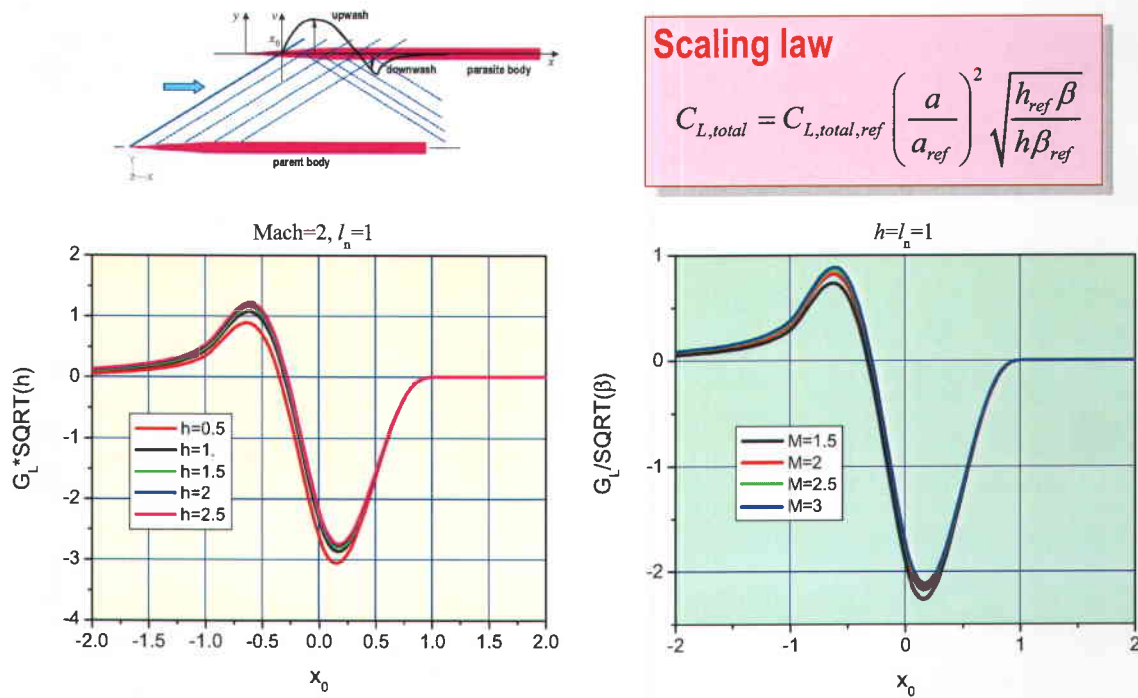

Figure 12 Scaling issue for interference between two identical bodies of revolution.

The aforementioned modeling has been carried out in the framework of the quasi-steady approximation. However, there are cases when acceleration of the body center of gravity and/or the pitching angular velocity are not small and the unsteady effects become appreciable. In FY 2007, we started a mathematical modeling of these effects. As a first step we considered the wave drag associated with unsteady motion of a slender body of revolution as shown in Figure 13.
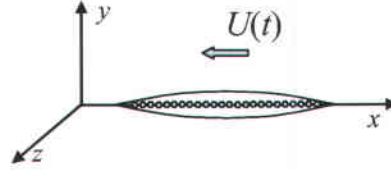
Figure 13 Slender body of revolution moving along x-axis with speed $U(t)$.

It is assumed that the body-induced disturbance is small compared with speed of sound, and the analysis is based on the linearized 3-D Euler equations. The disturbance velocity potential $\phi(x,y,z,t)$ is governed by the wave equation

$$\nabla^2\phi - \frac{1}{a_\infty^2}\frac{\partial^2\phi}{\partial t^2} = 0, \tag{1}$$

where a_∞ is speed of sound in undisturbed fluid. A slender body moving along the x-axis induces unsteady acoustic sources whose intensity $Q(x,t)$ is coupled with the body shape and motion as $Q(x,t) = \partial A_b(x,t)/\partial t$, where $A_b(x,t) = \pi r_b^2(x,t)$ is the body cross-sectional area. For the body of constant shape and length L moving with the velocity $U(t)$, we have $A_b(x,t) = A_b(X)$, where $X = x + \int_0^t U(\tau)d\tau$, $0 < X < L$, the solution is expressed in terms of the retarded potential as [21,24]

$$\phi(x,y,z,t) = -\frac{1}{4\pi}\int_{-\infty}^{\infty}\frac{U(\tau)A_b'(\eta)}{\sqrt{(x-\xi)^2+r^2}}d\xi, \tag{2}$$

$$\tau = t - \frac{\sqrt{(x-\xi)^2+r^2}}{a_\infty}, \quad \eta = \xi + \int_0^\tau U(\tau')d\tau', \quad r = \sqrt{y^2+z^2}. \tag{3}$$

The pressure distribution on the body surface is calculated using the near-field potential $\phi(x,r \to 0,t)$ and the unsteady Bernoulli equation in the slender-body approximation.

We considered an instantaneous acceleration of the body to a certain constant speed U at the initial time $t = 0$ and analyzed the wave drag $D(t)$ during the transient process. Figure 14 shows trajectories (black lines) of the body leading and trailing edges, the typical regions A, B and C associated with phases of the transient process as well as characteristics (red dashed lines) and end points $x_{1,2}$ typifying each phase. Analytical expressions for the wave drag $D(t)$ were derived for each of the aforementioned phases. Using these expressions $D(t)$ was calculated and compared with unsteady Euler CFD solution for the body of shape $r_b(X) = r_{max}\sin(\pi X/L)$,

13

$r_{max} = 0.01L$ at the Mach number $M = U/a_\infty = 2$ (Figure 15). The theoretical solution is in excellent agreement with CFD. This analysis provides a launching pad for theoretical modeling of the unsteady body motion accounting for the coupling between body dynamics and aerodynamics.
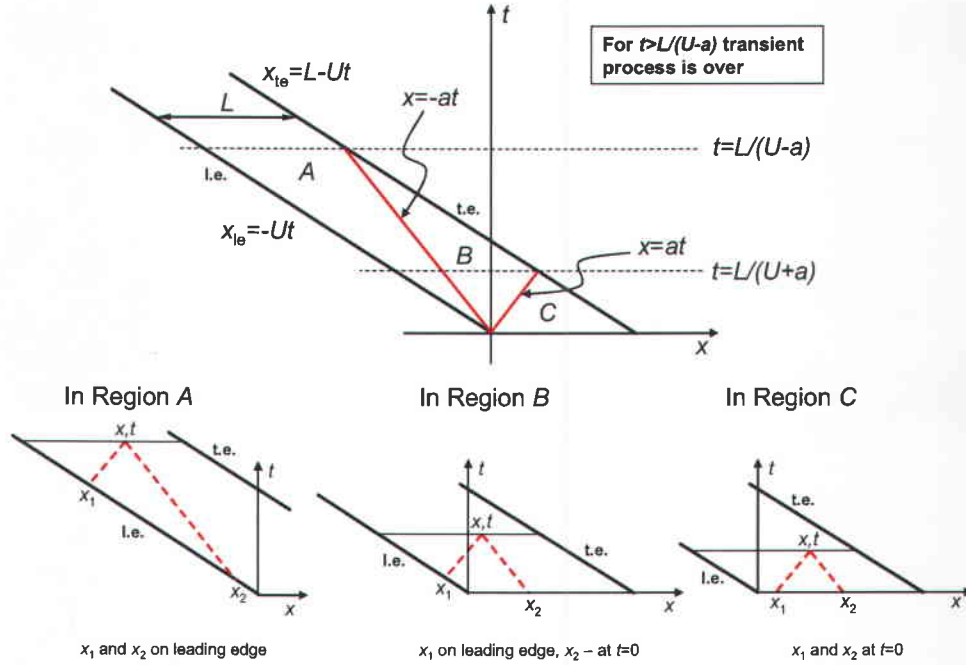
Details of this study are given in Appendix A.

Figure 14 Characteristics lines and boundaries for a slender body accelerating to a supersonic speed U at the initial time moment $t = 0$; here $a = a_\infty$, at $t = 0$ the body leading edge $x_{le}(0) = 0$ and the trailing edge $x_{te}(0) = L$.
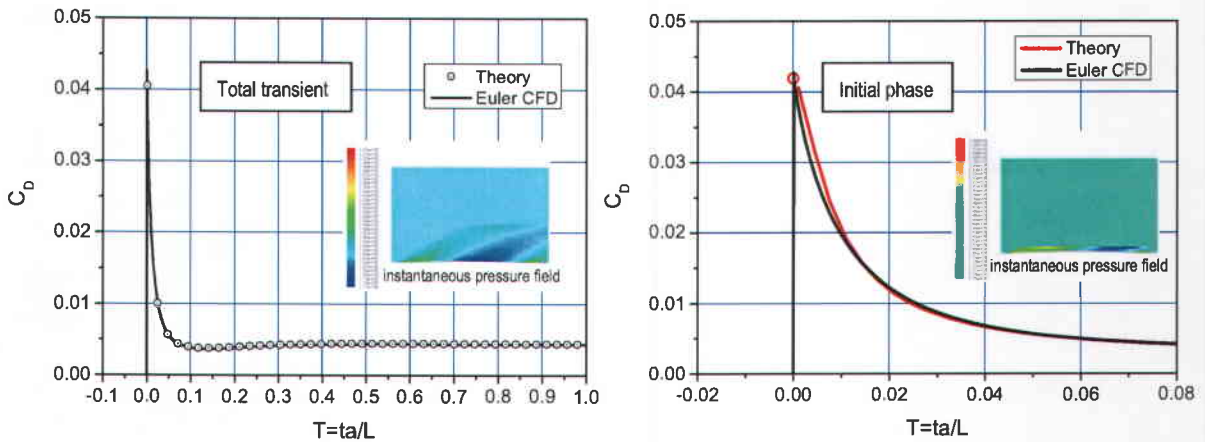
Figure 15 Comparison of theoretical and CFD history of drag coefficient $C_D(T)$, $C_D(T) = D(T)/\left(A_{max}\rho_\infty U^2/2\right)$, $T = ta_\infty/L$.

Our experience in low-order modeling of store separation helped Dr. Malmuth to develop a physics-based model for quick estimates of the body trajectory in the case of separation from a rectangular cavity to supersonic outer flow. The cavity is assumed to be deep with the shear layer bridging the front and rare cavity lips (open cavity flow). 3-DOF equations for the body motion includes aerodynamic loads (drag, lift and pitch moment), which are evaluated analytically and numerically for the three pahses of separation:

1. Body moves incide cavity
2. Body crosses shear layer
3. Body moves outside cavity in supersonic flow

In Phase 1, the body experiences aerodynamic loads due to the flow circulation inside the cavity and due to the body motion. Estimates based on viscous flow physics showed that these loads are of ther order of $O(\text{Re}_L^{-1}) + O(\beta^2)$, where Re_L is Reynolds number based on free-stream parameters and L=forebody length+cavity length, $\beta = v_e/U$ is ratio of the body vertical velocity to the freestream speed. For many practical cases, these parameters are small, and the aerodynamic loads incide cavity can be ignored. The body dynamic equations have a simple analytical solution relevant to the free drop in vacuum.

In Phase 2, the shear layer is assumed to be much thiner than the body radius and it is approximated by a straight line bridging the front and rare cavity lips. In addition, the body thickness ratio, ε, is treated as a small parameter (slender body approximation). With these assumptions, the aerodynamic loads are expressed in analytical forms using the method of matched asymptotic expansions.

In Phase 3, the equations for the body trajectory are solved analytically in the first-oreder approximation with respect to small parameters ε and β. This solution captures an osccilatory behavior of the pitch angle that depends on the aerodynamic coefficient $C_{m\alpha}$ (the pitch moment coefficient derivative with respect to angle of attack).
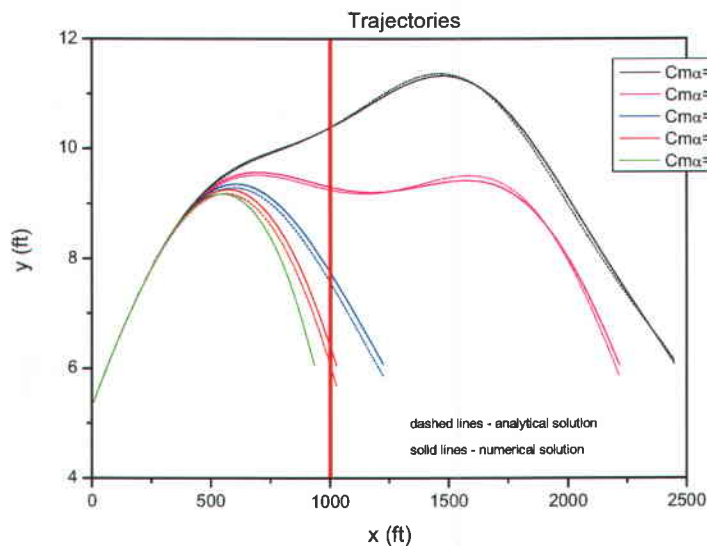

Figure 16 Trajectories at various $C_{m\alpha}$, free-stream Mach number=2.

As an example, Figure 16 shows the body trajectories at different values of $C_{m\alpha}$. Flow and body parameters are relevant to the HIFEX sled test [25]. As $C_{m\alpha}$ tends to zero, the pitch angle θ evolves from oscillatory to monotonic behavior versus x. Ultimately, θ becomes a linear function of time at $C_{m\alpha} = 0$ that gives monotonic decreasing of θ with x (the green line). Note that analytical solutions (dashed lines) are close to numerical ones (solid lines) in all cases considered.

Similar parametric calculations showed that models would hit the diverter and would not damage the test track (see Figure 17). This analysis along with other numerical studies of Boeing convinced the Air Force that the HIFEX store release was not a high-risk event and gave Boeing the go-ahead for the sled mission. Details of these studies can be given by Bill Bower (Boeing).

• **Theoretical model allows quick parametric studies of body trajectories**
• **It was shown that the store would not hit the track**

Mach 2 rocket sled configuration*

When models are released from the HIFEX bay, it is necessary to ensure that they do not damage the test track*

Arrangement of HIFEX weapons bay and MK-82 JDAM models for grid testing in the Boeing Polysonic Wind Tunnel*

*W.W. Bower, V. Kibens, A.W. Cary, G. Raman, and N. Malmuth, AIAA-2004-2513

Figure 17 Physics-based model helps to estimate store trajectories and shows that models released from the HIFEX bay do not damage the test track (HIFEX program).

3. Summary and impact of effort

In summary, new deductive asymptotic framework has been developed to treat the interaction between two supersonic bodies. Compact, closed-form analytical solutions were obtained for the two-body supersonic interference. These solutions are ideally suited for preliminary design, scaling and separation motor payload safety compromise that are not available from purely numerical solutions. They also provide a launching pad for systematic refinements and coupled

dynamic/aerodynamic modeling needed for staging tradeoff studies. Our theoretical model indicated that there are two physical mechanisms that control the interference flow field:

- Streamwise stratification of the transverse velocity imposed from one body on the other (mutual induction)

- Shock scattering from one body incident on the other

The aforementioned analysis provides for the first time an approximate but coherent picture of the wave train structure occurring in multi-body interference problems such as supersonic stage separation and flight crew escape. This is particularly important for internal carriage and cocoon release where shear layers bounding cavities exist. Moreover, this work provides a launching pad for the effort to obtain more understanding of the near field as well as increased prediction accuracy. This will strongly impact ejection system design and safe separation flow control.

Bill Bower of Boeing is using our store prediction and control expertise for HIFEX and SEAR programs.

In the case of superlight bodies, when acceleration of the body C.G. and/or the pitching angular velocity are not small, the unsteady effects become appreciable. First steps in mathematical modeling of these effects have been made with emphasis on the body wave drag. Namely, theoretical analysis of the wave drag generated by a non-lifting slender body of revolution during its instantaneous supersonic start was carried out. Typical phases of the transient process were identified. For each phase, analytical solutions of the flow potential and wave drag were obtained. The transient process was also simulated numerically by solving 3-D Euler equations. The theoretical wave drag is in excellent agreement with CFD in all phases of the transient process. These results provide a solid foundation for theoretical modeling of unsteady body motions including the coupling between body dynamics and aerodynamics.

References

[1]   Goodwin, F.K., Dillenius, M.F.E., and Nielsen, J.N., "Prediction of six-degree-of-freedom parasite body separation trajectories at speeds up to the critical speed. V.1. Theoretical methods and comparison with experiment". AFFDL-TR-72-83.

[2]   Wood, M.E., "Application of Experimental Techniques to Parasite body Release Problems". Proceedings of NEAR Conference on Missile Aerodynamics, Monterey, California, 1988.

[3]   Nielsen, J. N. *Missile Aerodynamics*. McGraw-Hill Company, Inc., New York, 1960.

[4]   Stanek, M.J., Sinha, N., Ahuja, V., Birkbeck, R.M. "Acoustic-Compatible Active Flow Control for Optimal Parasite body Separation," AIAA Paper No. 99-1911, 1999.

[5]   Malmuth, N.D., Fedorov, A.V., Shalaev, V., Cole, J., Khokhlov, A., Hites, M., and Williams, D., "Problems in High Speed Flow Prediction Relevant to Control," AIAA Paper No. 98-2695, 2nd AIAA Theoretical Fluid Dynamics Meeting, June 15-18, 1998, Albuquerque, NM.

[6]   Malmuth, N., Fedorov, A., Shalaev, V., Cole, J., Hites, M., and Williams, D. "Desktop Aerodynamic Models for Parasite body Separation from Parasite bodies Bay Cavities and

Related Vortical Processes," Vortex Flow at High Angle Attack, AVT Symposium, Paper 37, Loen, Norway, May 7-11, 2001.

[7] Malmuth, N.D., Shalaev, V.I., and Fedorov, A.V., "Combined Asymptotics and Numerical Methods for Parasite body Interactions," Technical Report of Contract CF49620-96-C-0004, AFOSR/NM, October 1998 (available in Defense Technical Information Center, stient.dtic.mil).

[8] Malmuth, N., Hites, M., and Williams, D., "Photographic Investigation of the Dynamics of an Ogive Model near a Cavity at Subsonic Mach Numbers," Final Report. Fluid Dynamics Research Center Illinois Institute of Technology, January 18, 1998.

[9] Shalaev, V.I., Fedorov, A.V., and Malmuth, N.D., "Dynamics of Slender Bodies Separating from Rectangular Cavities," AIAA Paper No. 2001-2996, 31 AIAA Fluid Dynamics Conference and Exhibit, 11-14 June 2001, *AIAA J.,* **40**(3), p. 517-525, 2002.

[10] Malmuth, N.D., Shalaev, V., and Fedorov, A, "Theoretical Analysis of Flow Between Two Supersonic Slender Bodies," Rockwell Scientific Company, Report NM03-24892, December 2003.

[11] Shalaev, V. Malmuth, N., and Fedorov. A., "Analytical Modeling of Transonic Parasite body Separation from a Cavity," AIAA Paper No. 2003-0004, 2003.

[12] Malmuth, N., Shalaev, V. and Fedorov, A. "A PC-Oriented Method to Estimate Parasite body Trajectories," presented at Aircraft-Parasite bodies Compatibility Symposium XIII, Eglin AFB, February 2003.

[13] Malmuth, N., and Shalaev, V., "Theoretical Modeling of Slender Bodies Interaction in Supersonic Flows," AIAA Paper No. 2004-1127 AIAA 42st Aerospace Sciences Meeting and Exhibit, Reno, Nevada, January 6, 2004.

[14] Malmuth, N.D., "Theoretical Aerodynamics in Today's Real World, Opportunities and Challenges," Julian D. Cole Lecture. AIAA Paper No. 2005-5059, 2005.

[15] Fedorov, A.V., Malmuth, N.D., and Soudakov, V.G., "Supersonic Scattering of a Wing-Induced Incident Shock by a Slender Body of Revolution," *J. Fluid Mech.*, **585**, 2007, pp. 305-322.

[16] Malmuth, N., Shalaev, V., and Fedorov, A., "Theoretical Analysis of Flow Between Two Supersonic Slender Bodies," Rockwell Scientific Company, Report NM03-24892, 2003.

[17] Morse, P., and Feshbach, H. *Methods of Theoretical Physics*, Vol. II, P. 1380, McGraw Hill, New York, 1953.

[18] Lependin, L. F. *Acoustics*. Vysshaya Shkola, Moscow, 1978 (in Russian).

[19] Bouche, D., Molinet, F., and Mittra, R. *Asymptotic Methods in Electromagnetics*, Springer-Verlag, New York, 1997.

[20] van Dyke, M. *Perturbation Methods in Fluid Mechanics*. Academic, 1964.

[21] Cole, J.D., and Cook, L.P. *Transonic Aerodymamics*. Elsevier Science Publishers B.V., 1986.

[22] Gapcynski, J.P., and Carlson, H.W., "The Aerodynamic Characteristics of a Body in the Two-Dimensional Flow Field of a Circular-Arc Wing at a Mach Number 2.01," NACA RM L57E14, Washington, July 2 1957.

[23] Fedorov, A.V., and Malmuth, N.D., "Theoretical Modeling of Two-Body Interaction in Supersonic Flow," invited - 5th AIAA Theoretical Fluid Mechanics Conference, Seattle, June 2008.

[24] Crow, S.C., and Bergmeier, G.G., "Active Sonic Boom Control," *J. Fluid Mech.*, **325**, 1996, pp. 1-28.

[25] Bower, W.W., Kibens, V., Cary, A.W., Alvi, F.S., Raman, G., Annaswamy, A., and Malmuth, N.D., "High-Frequency Excitation Flow Control for High-Speed Weppon Release (HIFEX)," AIAA Paper No. 2004-2513, 2004.

Publications (selected)

"Theoretical Aerodynamics in Today's Real World, Opportunities and Challenges," N. Malmuth, Julian D. Cole Lecture, *AIAA J.*, **44**, No.7, 2006, pp. 1377-1392.

"Supersonic Scattering of a Wing-Induced Incident Shock by a Slender Body of Revolution," A. V. Fedorov, N. D. Malmuth, and V. G. Soudakov, *J. Fluid Mech.*, **585**, 2007, pp. 305-322.

"Hypersonic Laminar Flow Control Using a Porous Coating of Random Microstructure," A. Maslov, A. Shiplyuk, A. Sidorenko, P. Polivanov, A. Fedorov, V. Kozlov, and M Malmuth, AIAA Paper No. 2006-1112, 2006.

"Acoustic Properties of Rarefied Gases Inside Pores of Simple Geometry, V. Kozlov, A. Fedorov, and N. Malmuth," *J. Acoust. Soc. Am.*, **117**, No. 6, 2005.

"Thin Shock Layer Model for a Jet in a Hypersonic Cross Flow," N. Malmuth, and A. Fedorov, AIAA Paper No. 2005-893, 2005.

"Wave Drag of Transonic Airplanes," J. Cole, and N. Malmuth., *Proc. Roy, Soc. A.*, **461**, No. 2054, Feb. 2005, pp.541-560.

"Theoretical Modeling of Slender Bodies Interaction in Supersonic Flows," AIAA Paper No. 2004-1127, 2004.

Fedorov, A.V., and Malmuth, N.D., "Theoretical Modeling of Two-Body Interaction in Supersonic Flow," invited - 5th AIAA Theoretical Fluid Mechanics Conference, Seattle, June 2008.

Appendix A: Wave Drag of a Slender Non-Lifting Body during Transient Process of Instanteneous Supersonic Start

1. Acoustic theory for a slender non-lifting body

Consider a slender body of revolution moving with an unsteady speed $U(t)$ at zero angle of attack along the x-axis as shown in Figure A1.
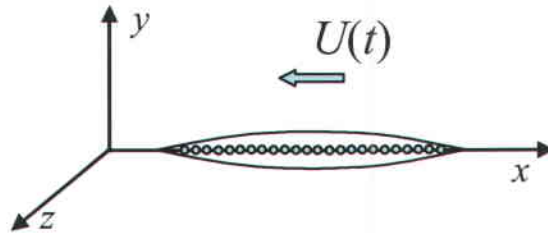
Figure A1 Slender body of revolution moving along the x-axis with speed $U(t)$.

Let $\mathbf{q}(x,y,z,t)$ - velocity disturbance induced by the body motion in gas at rest. It is assumed that this disturbance is small: $|\mathbf{q}|/a_\infty \ll 1$, where a_∞ is speed of sound in undisturbed gas at the infinity. The body-induced disturbances are treated as acoustic disturbances and governed by the linearized 3-D Euler equations of acoustic theory

$$\frac{\partial \rho}{\partial t} + \nabla \cdot \rho \mathbf{q} = 0,\tag{1.1a}$$

$$\rho\left(\frac{\partial \mathbf{q}}{\partial t} + \mathbf{q}\cdot\nabla\mathbf{q}\right) = -\nabla P,\tag{1.1b}$$

$$\frac{P}{\rho^\gamma} = \frac{P_\infty}{\rho_\infty^\gamma},\tag{1.1c}$$

where γ is specific heat ratio. For the disturbance velocity potential $\phi(x,y,z,t)$: $\mathbf{q}(x,y,z,t) = \nabla\phi$, we obtain the wave equation

$$\nabla^2\phi - \frac{1}{a_\infty^2}\frac{\partial^2\phi}{\partial t^2} = 0, \quad a_\infty^2 = \gamma\frac{P_\infty}{\rho_\infty}.\tag{1.2}$$

Disturbances of pressure, $\bar{p} = (P - P_\infty)/P_\infty$, and density, $\bar{s} = (\rho - \rho_\infty)/\rho_\infty$, are expressed as

$$\bar{p} = \gamma\bar{s} = -\frac{\rho_\infty}{P_\infty}\frac{\partial\phi}{\partial t}.\tag{1.3}$$

A pointed spherical source, which is located at $(x,y,z) = (0,0,0)$, generates a spherical wave with the potential

$$\phi(R,t)=\frac{f(t-R/a_\infty)}{R}, \quad R=\sqrt{x^2+y^2+z^2}.$$ (1.4)

This spherical wave induces the radial velocity

$$q_R(R,t)=\frac{\partial\phi}{\partial R}=-\frac{f(t-R/a_\infty)}{R^2}-\frac{f'(t-R/a_\infty)}{a_\infty R}.$$ (1.5)

The first term of (1.5) gives the near field and the second – the far field. For $R\to 0$, the mass flux perturbation (in units of ρ_∞) is

$$\lim_{x\to\infty}4\pi R^2 q_R(R,t)=-4\pi f(t)=Q(t),$$ (1.6)

where $Q(t)$ – the source intensity. For the impulse source, $Q(t)=\delta(t)$, we obtain

$$\phi(R,t)=-\frac{1}{4\pi}\frac{\delta(t-R/a_\infty)}{R}.$$ (1.7)

(1.7) is solution of the problem

$$\nabla^2\phi-\frac{1}{a_\infty^2}\frac{\partial^2\phi}{\partial t^2}=\delta(x)\delta(y)\delta(z)\delta(t),$$ (1.8a)

$$\phi=\frac{\partial\phi}{\partial t}=0 \text{ at } t=-0.$$ (1.8b)

The body induces unsteady acoustic sources with the source intensity depending on the body shape and motion. If $Q(x,t)$ is the source intensity at a point (x,t), then in accord with (1.7)

$$-4\pi\phi(x,y,z,t)=\int_{-\infty}^{t}d\tau\int_{-\infty}^{\infty}\frac{Q(\xi,\tau)\delta\left(t-\tau-\dfrac{R}{a_\infty}\right)}{R}d\xi,$$ (1.9a)

$$R=\sqrt{(x-\xi)^2+y^2+z^2}.$$ (1.9b)

Integrating over τ we obtain

$$-4\pi\phi(x,y,z,t)=\int_{-\infty}^{\infty}\frac{Q\left(\xi,t-\dfrac{\sqrt{(x-\xi)^2+r^2}}{a_\infty}\right)}{\sqrt{(x-\xi)^2+r^2}}d\xi,$$ (1.10a)

$$r=\sqrt{y^2+z^2}.$$ (1.10b)

The flow potential at (x,r,t) is induced by sources that were active at early time instants $\tau=t-\dfrac{R}{a_\infty}$. These sources are located on the hyperbola $\tau=t-\dfrac{\sqrt{(x-\xi)^2+r^2}}{a_\infty}$ between trajectories of the leading and trailing edges of the body as schematically shown in Figure A2.
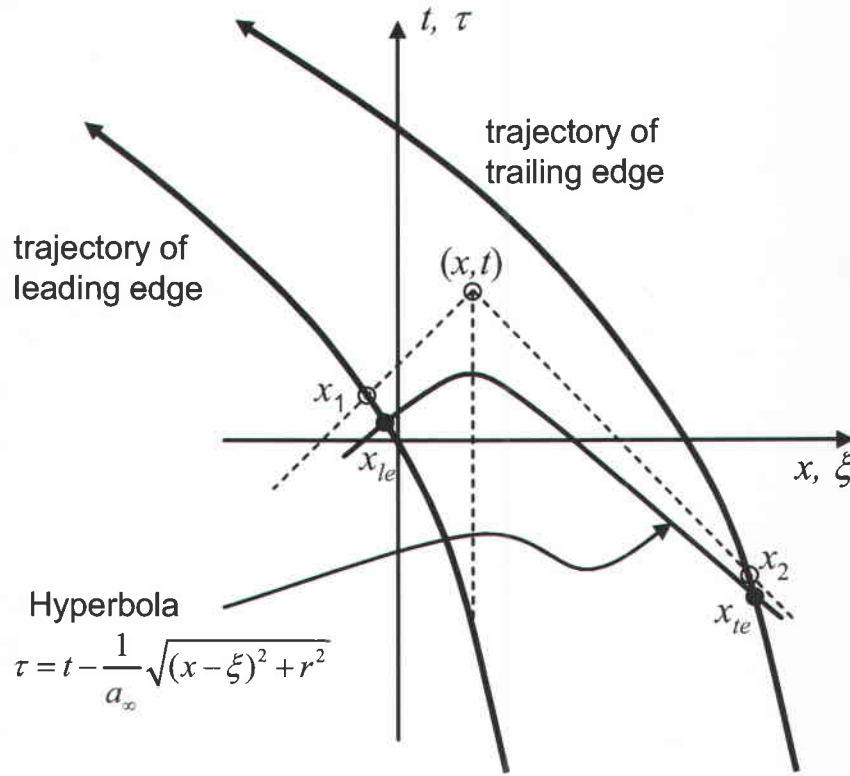
Figure A2 Influence domain for accelerating body.

Following Ref. [1] we consider asymptotic behavior of the integral (1.10a) for $r \to 0$. In this limit, the dominant contribution is associated with the vicinity of $\xi = x$. The integral (1.10a) is expressed as a sum of three integrals

$$\phi(x,r,t) = \phi_I + \phi_{II} + \phi_{III}, \tag{1.11}$$

$$-4\pi\phi_I(x,r,t) = \int_{x_{le}(x,r,t)}^{x-\varepsilon(r)} \frac{Q\left(\xi, t - \dfrac{\sqrt{(x-\xi)^2 + r^2}}{a_\infty}\right)}{\sqrt{(x-\xi)^2 + r^2}} d\xi, \tag{1.12}$$

$$-4\pi\phi_{II}(x,r,t) = \int_{x-\varepsilon(r)}^{x+\varepsilon(r)} \frac{Q\left(\xi, t - \dfrac{\sqrt{(x-\xi)^2 + r^2}}{a_\infty}\right)}{\sqrt{(x-\xi)^2 + r^2}} d\xi, \tag{1.13}$$

$$-4\pi\phi_{III}(x,r,t) = \int_{x+\varepsilon(r)}^{x_{te}(x,r,t)} \frac{Q\left(\xi, t - \dfrac{\sqrt{(x-\xi)^2 + r^2}}{a_\infty}\right)}{\sqrt{(x-\xi)^2 + r^2}} d\xi. \tag{1.14}$$

iii

With the substitution $\xi = x + r \sinh \sigma$, the second integral is written as

$$-4\pi\phi_{II}(x,r,t) = \int_{-\sigma_{II}}^{\sigma_{II}} Q\left(x + r\sinh\sigma, t - \frac{r\cosh\sigma}{a_\infty}\right) d\sigma, \qquad (1.15)$$

$$\sigma_{II} = \sinh^{-1}(\varepsilon/r).$$

Consider a distinguished limit $\varepsilon(r) \to 0 : r/\varepsilon \to 0$ for $r \to 0$. Then (1.15) is expanded as

$$-4\pi\phi_{II}(x,r,t) = \int_{-\sigma_{II}}^{\sigma_{II}} \left[Q(x,t) + r\sinh\sigma Q_x(x,t) - \frac{r\cosh\sigma}{a_\infty} Q_t(x,t) + \ldots \right] d\sigma =$$

$$2Q(x,t)\sinh^{-1}\left(\frac{\varepsilon}{r}\right) + O(\varepsilon) = 2Q(x,t)\log\left(\frac{\varepsilon}{r} + \sqrt{\frac{\varepsilon^2}{r^2} + 1}\right) + O(\varepsilon) = \qquad (1.16)$$

$$2Q(x,t)\log\frac{2\varepsilon}{r} + O\left(\varepsilon, \frac{r^2}{\varepsilon^2}\right)$$

Consider the first integral (1.12). Integrating by parts we get

$$-4\pi\phi_I(x,r,t) = \int_{x_{le}(x,r,t)}^{x-\varepsilon(r)} \frac{Q\left(\xi, t - \frac{x-\xi}{a_\infty}\right)}{(x-\xi)} d\xi + \ldots =$$

$$Q\left(x_1, t - \frac{x-x_1}{a_\infty}\right)\log(x-x_1) - Q(x,t)\log\varepsilon - \int_{x_1}^{x}\log(x-\xi)\left[Q_x\left(\xi, t - \frac{x-\xi}{a_\infty}\right) + \frac{1}{a_\infty}Q_t\left(\xi, t - \frac{x-\xi}{a_\infty}\right)\right]d\xi$$

$$(1.17)$$

where $x_1(x,t) = x_{le}(x,0,t)$ is shown in Figure A2 (see intersection of the dashed line with the leading-edge trajectory).

In a similar way

$$-4\pi\phi_{III}(x,r,t) = \int_{x-\varepsilon(r)}^{x_{te}(x,r,t)} \frac{Q\left(\xi, t - \frac{x-\xi}{a_\infty}\right)}{(x-\xi)} d\xi + \ldots =$$

$$Q\left(x_2, t - \frac{x_2-x}{a_\infty}\right)\log(x_2-x) - Q(x,t)\log\varepsilon + \int_{x}^{x_2}\log(\xi-x)\left[Q_x\left(\xi, t - \frac{\xi-x}{a_\infty}\right) - \frac{1}{a_\infty}Q_t\left(\xi, t - \frac{\xi-x}{a_\infty}\right)\right]d\xi$$

$$(1.18)$$

where $x_2(x,t) = x_{te}(x,0,t)$ is intersection of the dashed line with the trailing-edge trajectory (Figure A2). The final expression for the flow potential in the vicinity of slender body is

iv

$$-4\pi\phi(x,r,t) = 2Q(x,t)\log\frac{2}{r}$$

$$+Q_1\log(x-x_1)+Q_2\log(x_2-x)$$

$$+\int_{x_1}^{x}\log(x-\xi)\left\{Q_x+\frac{1}{a_\infty}Q_t\right\}_d d\xi - \int_{x}^{x_2}\log(\xi-x)\left\{Q_x-\frac{1}{a_\infty}Q_t\right\}_d d\xi$$

$$+O(r^2\log r)$$

(1.19)

where

$$Q_1 = Q\left(x_1,t-\frac{x-x_1}{a_\infty}\right),\quad Q_2 = Q\left(x_2,t-\frac{x_2-x}{a_\infty}\right),$$

(1.20)

$$\{f\}_d \equiv f\left(\xi,t-\frac{|x-\xi|}{a_\infty}\right),$$

(1.21)

$$x_1(x,t) = x_{le}(x,0,t),\quad x_2(x,t) = x_{te}(x,0,t).$$

(1.22)

Note that the solution (1.19) coincides with the solution (2) of Ref. [2].

Now we can couple the source intensity $Q(x,t)$ with the body motion by imposing the boundary condition on the body surface. For the body shape

$$B(x,r,t) = 0 = r - r_b(x,t),$$

(1.23)

the boundary condition reads

$$\frac{\partial B}{\partial t} + \mathbf{q}\cdot\nabla B = 0 \text{ at } B = 0.$$

(1.24)

This gives

$$-\frac{\partial r_b}{\partial t} - \phi_x\frac{\partial r_b}{\partial x} + \phi_r = 0 \text{ at } r = r_b(x,t),$$

(1.25)

where r_b is body radius. In the first-order approximation, we obtain

$$\phi_r(x,r_b,t) = \frac{\partial r_b}{\partial t}.$$

(1.26)

Using (1.19), which was derived for small r, we get

$$Q(x,t) = \frac{\partial A_b(x,t)}{\partial t},$$

(1.27)

where $A_b(x,t) = \pi r_b^2(x,t)$ is the body cross-sectional area.

For a body of constant shape and length L moving with velocity $U(t)$, we have

$$A_b(x,t) = A_b(X),\ 0 < X < L,$$

(1.28a)

$$X = x + \int_0^t U(\tau)d\tau .$$

(1.28b)

In this case

$$Q(x,t) = \frac{\partial A_b(x,t)}{\partial t} = \frac{dA_b}{dX}\frac{\partial X}{\partial t} = U(t)A_b'(X) .$$

(1.29)

Substitution of (1.29) into (1.10a) gives

$$\phi(x,y,z,t) = -\frac{1}{4\pi}\int_{-\infty}^{\infty}\frac{\frac{\partial A_b}{\partial \tau}(\xi,\tau)}{\sqrt{(x-\xi)^2 + r^2}}d\xi ,$$

(1.30a)

$$\tau = t - \frac{\sqrt{(x-\xi)^2 + r^2}}{a_\infty} .$$

(1.30b)

Note that this expression coincides with (1.3.11) of [3].

2. Analysis of the wave drag

The wave drag can be also calculated using the near-filed potential $\phi(x,r\rightarrow 0,t)$ given by (1.19), and the unsteady Bernoulli equation. For a slender body ($r\rightarrow 0$), the Bernoulli equation reads

$$p \equiv P - P_\infty = -\rho_\infty\left[\frac{\partial \phi}{\partial t} + \frac{1}{2}\left(\frac{\partial \phi}{\partial r}\right)^2\right],$$

(2.2)

and the wave drag is calculated as

$$D(t) = \int_0^L p_w(X,t)A_b'(X)dX ,$$

(2.3)

where X is measured from the body leading edge, and the pressure p_w is calculated on the body surface.

Herein we consider an instantaneous acceleration of the body to a certain constant speed U at the initial time moment $t = 0$ and analyze the wave drag $D(t)$ during the transient process. Hereafter we consider the supersonic case $U > a_\infty$ following the plan:

1. Identify typical phases of the transient process and determine the end points $x_{1,2}$ (see Figure A2) associated with the basic expression (1.19) for the flow potential
2. Using (1.19) calculate the near-filed flow potential for each phase
3. Using (2.2) calculate the wall pressure $p_w(X,t)$
4. Using (2.3) calculate the wave drag $D(t)$

2.1 Structure of the influence domain

Figure A3 shows trajectories of the leading and trailing edges, the typical regions A, B and C associated with phases of the transient process as well as locations of characteristics and end points $x_{1,2}$ for each phase.

1. If the point (x,t) lies in Region A, the end points $x_{1,2}$ are at the body leading and trailing edges. The wall pressure $p_w(x,t) = p_{w,A}(X)$ should correspond to a steady flight with supersonic speed U.

2. If the point (x,t) lies in Region B, then x_1 is at the leading edge, while x_2 lies on the body axis at $t = 0$. Here the wall pressure $p_w(x,t) = p_{w,B}(X,t)$ is unsteady.

3. In Region C, the end points $x_{1,2}$ are on the body axis at $t = 0$, and the wall pressure $p_w(x,t) = p_{w,C}(X,t)$ is unsteady.

In Region A In Region B In Region C

x_1 and x_2 on leading edge x_1 on leading edge, x_2 – at $t=0$ x_1 and x_2 at $t=0$
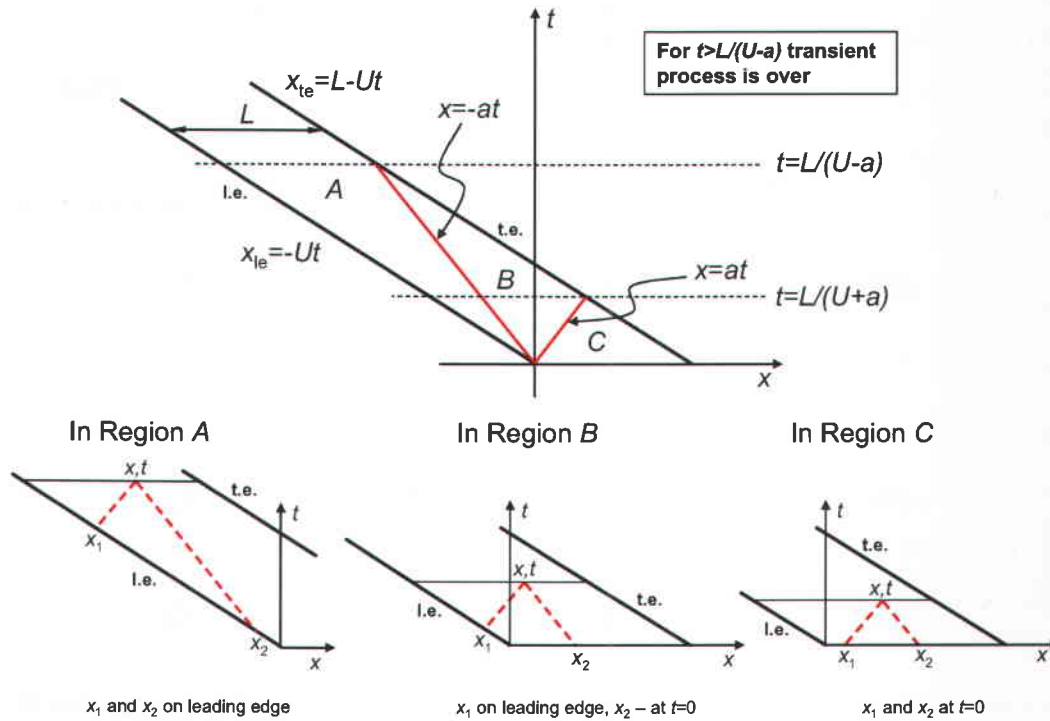
Figure A3 Characteristic lines and boundaries for a slander body accelerating to a supersonic speed U at the initial time moment $t = 0$; here $a = a_\infty$, at $t = 0$ the body leading edge $x_{le}(0) = 0$ and the trailing edge $x_{te}(0) = L$.

For $t > L/(U - a_\infty)$, the region A covers the total body length; i.e., the wall pressure corresponds to the steady flight allover the body length. The transient process is over and the wave drag should be given by the classic formula of von Karman and Moore [4]

$$D_A = -\frac{\rho_\infty U^2}{2\pi} \int_0^L A_b''(X) \left[\int_0^X \log(X - \sigma) A_b''(\sigma) d\sigma \right] dX . \qquad (2.4)$$

$$\xi = \frac{X_1 - Ut + Mx}{(1+M)}, \quad d\xi = \frac{dX_1}{(1+M)}, \quad X_1(\xi = x_{1A}) = 0, \quad X_1(\xi = x) = X, \quad x - \xi = \frac{X - X_1}{1+M}, \quad (2.12)$$

$$\xi = \frac{X_2 - Ut - Mx}{(1-M)}, \quad d\xi = \frac{dX_2}{(1-M)}, \quad X_2(\xi = x_{2A}) = 0, \quad X_2(\xi = x) = X, \quad \xi - x = \frac{X_2 - X}{1-M}. \quad (2.13)$$

Then the potential (2.11) is written as

$$\phi(x,r,t) = \frac{1}{2\pi} U A_b'(X) \log\frac{r}{2} -$$

$$-\frac{U}{4\pi}\int_0^X \log\left(\frac{X - X_1}{1+M}\right) A_b''(X_1) dX_1 + \frac{U}{4\pi}\int_X^0 \log\left(\frac{X_2 - X}{1-M}\right) A_b''(X_2) dX_2 +$$

$$+O(r^2 \log r) =$$

$$\frac{1}{2\pi} U A_b'(X) \log\frac{r}{2} -$$

$$-\frac{U}{4\pi}\int_0^X \log\left(\frac{X - X_1}{1+M}\right) A_b''(X_1) dX_1 - \frac{U}{4\pi}\int_0^X \log\left(\frac{X - X_2}{M-1}\right) A_b''(X_2) dX_2 +$$

$$+O(r^2 \log r) =$$

$$= \frac{1}{2\pi} U A_b'(X) \log\frac{r}{2} - \frac{U}{4\pi}\int_0^X \log\left[\frac{(X-\sigma)^2}{M^2-1}\right] A_b''(\sigma) d\sigma + O(r^2 \log r)$$

Finally we get for the near-filed potential at $(x,t) \in A$

$$\phi_A(x,r,t) = -\frac{U}{2\pi}\int_0^X \log\left(\frac{2(X-\sigma)}{r\beta}\right) A_b''(\sigma) d\sigma, \quad \beta \equiv \sqrt{M^2 - 1}. \quad (2.14)$$

Note that this potential coincides with the well known near-field potential for steady supersonic flight (see, for example, Ref. [5]).

2.2.2 Potential in Region B

In this region the end points are

$$x_{1B} = x_{1A} = \frac{U}{U + a_\infty}(x - a_\infty t), \quad x_{2B} = x + a_\infty t. \quad (2.15)$$

The sources are

$$Q_x \pm \frac{1}{a_\infty} Q_t = U(1 \pm M) A_b''(X), \quad (2.16)$$

$$\left\{ Q_x + \frac{1}{a_\infty} Q_t \right\}_d = U(1+M) A_b''(X_1), \quad X_1 = (1+M)\xi + Ut - Mx, \quad (2.17)$$

$$\left\{ Q_x - \frac{1}{a_\infty} Q_t \right\}_d = U(1-M)A_b''(X_2), \quad X_2 = (1-M)\xi + Ut + Mx. \tag{2.18}$$

Since $A_b'(0) = 0$ for body with a sharp nose, we have

$$Q_1 = 0, \quad Q_2 = UA_b'(x + a_\infty t). \tag{2.19}$$

Then, (1.19) gives

$$\phi_B(x,r,t) = -\frac{1}{4\pi} UA_b'(x + a_\infty t) \log a_\infty t + \frac{1}{2\pi} UA_b'(X) \log \frac{r}{2}$$

$$-\frac{U(1+M)}{4\pi} \int_{x_{1B}}^{x} \log(x - \xi) A_b''(X_1) d\xi + \frac{U(1-M)}{4\pi} \int_{x}^{x_{2B}} \log(\xi - x) A_b''(X_2) d\xi \tag{2.20}$$

$$+ O(r^2 \log r)$$

Equation (2.20) can be written as

$$\phi_B(x,r,t) = \phi_A(x,r,t) - \frac{1}{4\pi} UA_b'(x + a_\infty t) \log a_\infty t + \frac{U(1-M)}{4\pi} \int_{x_{2A}}^{x_{2B}} \log(\xi - x) A_b''(X_2) d\xi.$$

Using the new variable X_2, we get

$$\xi = \frac{X_2 - Ut - Mx}{(1-M)}, \quad d\xi = \frac{dX_2}{(1-M)}, \quad X_2(\xi = x_{2B}) = x + a_\infty t, \quad X_2(\xi = x_{2A}) = 0, \quad \xi - x = \frac{X_2 - X}{1-M}.$$

Then (2.20) is written as

$$\phi_B(x,r,t) = \phi_A(x,r,t) - \frac{U}{4\pi} A_b'(x + a_\infty t) \log a_\infty t + \frac{U}{4\pi} \int_{0}^{x+a_\infty t} \log\left(\frac{X - X_2}{M-1} \right) A_b''(X_2) dX_2 =$$

$$\phi_A(x,r,t) - \frac{U}{4\pi} A_b'(x + a_\infty t) \log\left[(U - a_\infty)t \right] + \frac{U}{4\pi} \int_{0}^{x+a_\infty t} \log(X - \sigma) A_b''(\sigma) d\sigma$$

Finally we obtain for $(x,t) \in B$

$$\phi_B(x,r,t) = \phi_A(x,r,t) - \frac{U}{4\pi} A_b'(x + a_\infty t) \log\left[(U - a_\infty)t \right] + \frac{U}{4\pi} \int_{0}^{x+a_\infty t} \log(X - \sigma) A_b''(\sigma) d\sigma. \tag{2.21}$$

2.2.3 Potential in Region C

Coordinates of the end points are

$$x_{1C} = x - a_\infty t, \quad x_{2C} = x + a_\infty t. \tag{2.22}$$

The sources are

$$Q_x \pm \frac{1}{a_\infty} Q_t = U(1 \pm M) A_b''(X), \tag{2.23}$$

x

$$\left\{Q_x + \frac{1}{a_\infty}Q_t\right\}_d = U(1+M)A_b''(X_1), \quad X_1 = (1+M)\xi + Ut - Mx, \tag{2.24}$$

$$\left\{Q_x - \frac{1}{a_\infty}Q_t\right\}_d = U(1-M)A_b''(X_2), \quad X_2 = (1-M)\xi + Ut + Mx, \tag{2.25}$$

$$Q_1 = UA_b'(x - a_\infty t), \quad Q_2 = UA_b'(x + a_\infty t). \tag{2.26}$$

Then, (1.19) gives

$$\phi_C(x,r,t) = -\frac{1}{4\pi}UA_b'(x - a_\infty t)\log a_\infty t - \frac{1}{4\pi}UA_b'(x + a_\infty t)\log a_\infty t$$

$$+ \frac{1}{2\pi}UA_b'(X)\log\frac{r}{2} - \frac{U(1+M)}{4\pi}\int_{x_{1C}}^{x}\log(x - \xi)A_b''(X_1)d\xi$$

$$+ \frac{U(1-M)}{4\pi}\int_{x}^{x_{2C}}\log(\xi - x)A_b''(X_2)d\xi + O(r^2\log r)$$

This expression can be written as

$$\phi_C(x,r,t) = \phi_A(x,r,t) - \frac{1}{4\pi}UA_b'(x - a_\infty t)\log a_\infty t - \frac{1}{4\pi}UA_b'(x + a_\infty t)\log a_\infty t$$

$$+ \frac{U(1+M)}{4\pi}\int_{x_{1A}}^{x_{1C}}\log(x - \xi)A_b''(X_1)d\xi + \frac{U(1-M)}{4\pi}\int_{x_{2A}}^{x_{2C}}\log(\xi - x)A_b''(X_2)d\xi \tag{2.27}$$

Using the new variables X_1 and X_2, we obtain

$$\xi = \frac{X_1 - Ut + Mx}{(1+M)}, \quad d\xi = \frac{dX_1}{(1+M)}, \quad X_1(\xi = x_{1A}) = 0, \quad X_1(\xi = x_{1C}) = x - a_\infty t, \quad x - \xi = \frac{X - X_1}{1+M},$$

$$\xi = \frac{X_2 - Ut - Mx}{(1-M)}, \quad d\xi = \frac{dX_2}{(1-M)}, \quad X_2(\xi = x_{2C}) = x + a_\infty t, \quad X_2(\xi = x_{2A}) = 0, \quad \xi - x = \frac{X_2 - X}{1-M}.$$

Then the potential (2.27) is expressed as

$$\phi_C(x,r,t) = \phi_B(x,r,t) - \frac{1}{4\pi}UA_b'(x - a_\infty t)\log a_\infty t + \frac{U}{4\pi}\int_{0}^{x - a_\infty t}\log\left(\frac{X - X_1}{M+1}\right)A_b''(X_1)dX_1 =$$

$$\phi_B(x,r,t) - \frac{U}{4\pi}A_b'(x - a_\infty t)\log\left[(U + a_\infty)t\right] + \frac{U}{4\pi}\int_{0}^{x - a_\infty t}\log\left(X - \sigma\right)A_b''(\sigma)d\sigma$$

Finally we get for $(x,t) \in C$

$$\phi_C(x,r,t) = \phi_B(x,r,t) - \frac{U}{4\pi}A_b'(x - a_\infty t)\log\left[(U + a_\infty)t\right] + \frac{U}{4\pi}\int_{0}^{x - a_\infty t}\log\left(X - \sigma\right)A_b''(\sigma)d\sigma. \tag{2.28}$$

2.3 Wave drag for $t > L/(U-a_\infty)$

Figure A3 shows that for $t > L/(U-a_\infty)$ the body is totally in Region A. Then

$$\phi_A = -\frac{U}{2\pi}\int_0^X \log\left(\frac{2(X-\sigma)}{r\beta}\right)A_b''(\sigma)d\sigma = \frac{U}{2\pi}\left[\int_0^X A_b''(\sigma)\log r\,d\sigma - \int_0^X \log\left(\frac{2(X-\sigma)}{\beta}\right)A_b''(\sigma)d\sigma\right]$$

(2.29)

$$\left.\frac{\partial \phi_A}{\partial r}\right|_{r=r_b(X)} = \frac{U}{2\pi}\frac{A_b'(X)}{r_b(X)}$$

(2.30)

$$\left.\frac{\partial \phi_A}{\partial t}\right|_{r=R(X)} = U\left.\frac{\partial \phi_A}{\partial X}\right|_{r=r_b(X)} = \frac{U^2}{2\pi}\left[A_b''(X)\log r_b(X) - \frac{\partial}{\partial X}\int_0^X \log\left(\frac{2(X-\sigma)}{\beta}\right)A_b''(\sigma)d\sigma\right]$$

(2.31)

The wall pressure in Region A is

$$p_{wA} = -\rho_\infty\left[\frac{\partial \phi_A}{\partial t} + \frac{1}{2}\left(\frac{\partial \phi_A}{\partial r}\right)^2\right]_{r=r_b} =$$

$$\frac{\rho_\infty U^2}{2\pi}\left[-A_b''(X)\log r_b(X) + \frac{\partial}{\partial X}\int_0^X \log\left(\frac{2(X-\sigma)}{\beta}\right)A_b''(\sigma)d\sigma - \frac{1}{4\pi}\left(\frac{A_b'(X)}{r_b(X)}\right)^2\right]$$

(2.32)

Substituting (2.32) into (2.3) we get the wave drag

$$\frac{2\pi D_A}{\rho_\infty U^2} = \int_0^L A_b'(X)\left[-A_b''(X)\log r_b(X) + \frac{\partial}{\partial X}\int_0^X \log\left(\frac{2(X-\sigma)}{\beta}\right)A_b''(\sigma)d\sigma - \frac{1}{4\pi}\left(\frac{A_b'(X)}{r_b(X)}\right)^2\right]dX .$$

Since $A_b' = 2\pi r_b r_b'$, we can combine the first and third terms as

$$-\int_0^L\left[A_b'(X)A_b''(X)\log r_b(X) + \frac{r_b'(X)}{2r_b(X)}[A_b'(X)]^2\right]dX = -\int_0^L\frac{d}{dX}\left[\frac{1}{2}A_b'^2(X)\log r_b(X)\right]dX = 0 ,$$

where we utilized the condition $A_b'(0) = A_b'(L) = 0$. The second term is integrated by parts as

$$\int_0^L\left[A_b'(X)\frac{\partial}{\partial X}\int_0^X \log\left(\frac{2(X-\sigma)}{\beta}\right)A_b''(\sigma)d\sigma\right]dX = -\int_0^L\left[A_b''(X)\int_0^X \log(X-\sigma)A_b''(\sigma)d\sigma\right]dX .$$

Finally we obtain the classic formula of Karman and Moore

$$D_A = -\frac{\rho_\infty U^2}{2\pi}\int_0^L\left[A_b''(X)\int_0^X \log(X-\sigma)A_b''(\sigma)d\sigma\right]dX =$$

$$= \frac{\rho_\infty U^2}{4\pi}\int_0^L\left[A_b''(X)\int_0^l \log\left(\frac{1}{|X-\sigma|}\right)A_b''(\sigma)d\sigma\right]dX$$

(2.33)

2.4 Wave drag for $L/(U+a_\infty) < t < L/(U-a_\infty)$

In this case, Region A corresponds to $0 < X < L_A$, and Region B corresponds to $L_A < X < L$, where $L_A = (U - a_\infty)t$. The wave drag is

$$D(t) = \int_0^{L_A} p_{wA}(X,t)A_b'(X)dX + \int_{L_A}^{L} p_{wB}(X,t)A_b'(X)dX = D_A + \int_{L_A}^{L}[p_{wB}(X,t) - p_{wA}(X,t)]A_b'(X)dX$$

where the difference $p_{wAB}(X,t) \equiv p_{wB}(X,t) - p_{wA}(X,t)$ is calculated using the flow potential

$$\phi_{AB} = \phi_B - \phi_A = -\frac{U}{4\pi}A_b'(x+a_\infty t)\log[(U-a_\infty)t] + \frac{U}{4\pi}\int_0^{x+a_\infty t}\log(X-\sigma)A_b''(\sigma)d\sigma. \quad (2.34)$$

Interestingly, the potential ϕ_{AB} does not depend on r. Then

$$p_{wAB} \equiv p_{wB} - p_{wA} = -\rho_\infty\frac{\partial\phi_{AB}}{\partial t} = \frac{\rho_\infty U}{4\pi}\left[a_\infty A_b''(x+a_\infty t)\log[(U-a_\infty)t] + \frac{A_b'(x+a_\infty t)}{t}\right] -$$

$$\frac{\rho_\infty U}{4\pi}\left[\int_0^{x+a_\infty t}\frac{UA_b''(\sigma)}{x+Ut-\sigma}d\sigma + a_\infty A_b''(x+a_\infty t)\log[(U-a_\infty)t]\right] =$$

$$\frac{\rho_\infty U}{4\pi}\left[\frac{A_b'(x+a_\infty t)}{t} - \int_0^{x+a_\infty t}\frac{UA_b''(\sigma)}{x+Ut-\sigma}d\sigma\right] = \frac{\rho_\infty U^2}{4\pi}\left[\frac{A_b'(X-(U-a_\infty)t)}{Ut} - \int_0^{X-(U-a_\infty)t}\frac{A_b''(\sigma)}{X-\sigma}d\sigma\right]$$

The wave drag component associated with this pressure difference is

$$D_{AB}(t) = \int_{L_A}^{L}[p_{wB}(X,t) - p_{wA}(X,t)]A_b'(X)dX =$$

$$\frac{\rho_\infty U^2}{4\pi}\int_{(U-a_\infty)t}^{L}\left[\frac{A_b'(X-(U-a_\infty)t)}{Ut} - \int_0^{X-(U-a_\infty)t}\frac{A_b''(\sigma)}{X-\sigma}d\sigma\right]A_b'(X)dX = \quad (2.35)$$

$$\frac{\rho_\infty U^2}{4\pi}\frac{1}{Ut}\int_{(U-a_\infty)t}^{L}A_b'(X-(U-a_\infty)t)A_b'(X)dX - \frac{\rho_\infty U^2}{4\pi}\int_{(U-a_\infty)t}^{L}\left[\int_0^{X-(U-a_\infty)t}\frac{A_b''(\sigma)}{X-\sigma}d\sigma\right]A_b'(X)dX$$

Then the wave drag is

$$D(t) = D_A + D_{AB}(t) \quad (2.36)$$

Note that the second integral in (2.35) is not singular since $(U-a_\infty)t < X - \sigma < X$, where $(U-a_\infty)t < X < L$ and $L/(U+a_\infty) < t < L/(U-a_\infty)$. As $t \to L/(U-a_\infty)$, the lower limit behaves as $(U-a_\infty)t \to L$, and both integrals tend to zero; i.e., the wave drag (2.36) is matched with D_A at the upper boundary $t = L/(U-a_\infty)$.

2.5 Wave drag for $0 < t < L/(U + a_\infty)$

In this case, Region A corresponds to $0 < X < L_A$, Region B corresponds to $L_A < X < L_B$, and Region C corresponds to $L_B < X < L$, where $L_A = (U - a_\infty)t$ and $L_B = (U + a_\infty)t$. The wave drag is

$$D(t) = \int_0^{L_A} p_{wA}(X,t)A_b'(X)dX + \int_{L_A}^{L_B} p_{wB}(X,t)A_b'(X)dX + \int_{L_B}^{L} p_{wC}(X,t)A_b'(X)dX =$$

$$= D_A + \int_{L_A}^{L} [p_{wB}(X,t) - p_{wA}(X,t)]A_b'(X)dX + \int_{L_B}^{L} [p_{wC}(X,t) - p_{wB}(X,t)]A_b'(X)dX = \quad (3.37)$$

$$= D_A + D_{AB}(t) + D_{BC}(t)$$

Here D_A is given by (2.33), $D_{AB}(t)$ is given by (3.35), and $D_{AC}(t)$ is calculated using the potential

$$\phi_{BC}(x,r,t) \equiv \phi_C - \phi_B = -\frac{U}{4\pi} A_b'(x - a_\infty t)\log\left[(U + a_\infty)t\right] + \frac{U}{4\pi}\int_0^{x-a_\infty t} \log\left(X - \sigma\right) A_b''(\sigma)d\sigma . \quad (2.38)$$

The wall pressure is expressed as

$$p_{wBC} = -\rho_\infty \frac{\partial \phi_{BC}}{\partial t} = \frac{\rho_\infty U}{4\pi}\left[-a_\infty A_b''(x - a_\infty t)\log[(U + a_\infty t)] + \frac{A_b'(x - a_\infty t)}{t} \right] -$$

$$\frac{\rho_\infty U}{4\pi}\left[\int_0^{x-a_\infty t} \frac{UA_b''(\sigma)}{x + Ut - \sigma}d\sigma - a_\infty A_b''(x - a_\infty t)\log[(U + a_\infty t)] \right] =$$

$$\frac{\rho_\infty U}{4\pi}\left[\frac{A_b'(x - a_\infty t)}{t} - \int_0^{x-a_\infty t} \frac{UA_b''(\sigma)}{x + Ut - \sigma}d\sigma \right] = \frac{\rho_\infty U^2}{4\pi}\left[\frac{A_b'(X - (U + a_\infty)t)}{Ut} - \int_0^{X-(U+a_\infty)t} \frac{A_b''(\sigma)}{X - \sigma}d\sigma \right]$$

$$D_{BC}(t) = \int_{L_B}^{L} [p_{wC}(X,t) - p_{wB}(X,t)]A_b'(X)dX =$$

$$\frac{\rho_\infty U^2}{4\pi} \int_{(U+a_\infty)t}^{L}\left[\frac{A_b'(X - (U + a_\infty)t)}{Ut} - \int_0^{X-(U+a_\infty)t} \frac{A_b''(\sigma)}{X - \sigma}d\sigma \right] A_b'(X)dX = \quad (2.39)$$

$$\frac{\rho_\infty U^2}{4\pi}\frac{1}{Ut} \int_{(U+a_\infty)t}^{L} A_b'(X - (U + a_\infty)t)A_b'(X)dX - \frac{\rho_\infty U^2}{4\pi} \int_{(U+a_\infty)t}^{L}\left[\int_0^{X-(U+a_\infty)t} \frac{A_b''(\sigma)}{X - \sigma}d\sigma \right] A_b'(X)dX$$

Finally we get

$$D(t) = D_A + D_{AB}(t) + D_{BC}(t) = D_A +$$

$$+ \frac{\rho_\infty U^2}{4\pi} \frac{1}{Ut} \int_{(U-a_\infty)t}^{L} A_b'(X - (U - a_\infty)t) A_b'(X) dX - \frac{\rho_\infty U^2}{4\pi} \int_{(U-a_\infty)t}^{L} \left[\int_0^{X-(U-a_\infty)t} \frac{A_b''(\sigma)}{X - \sigma} d\sigma \right] A_b'(X) dX +$$

$$+ \frac{\rho_\infty U^2}{4\pi} \frac{1}{Ut} \int_{(U+a_\infty)t}^{L} A_b'(X - (U + a_\infty)t) A_b'(X) dX - \frac{\rho_\infty U^2}{4\pi} \int_{(U+a_\infty)t}^{L} \left[\int_0^{X-(U+a_\infty)t} \frac{A_b''(\sigma)}{X - \sigma} d\sigma \right] A_b'(X) dX$$

$$(2.40)$$

2.6 Wave drag for $t \to 0$

For $t \to 0$, the components $D_{AB}(t)$ and $D_{BC}(t)$ need a special treatment, since the drag tends to infinity as

$$D(t) \to \frac{\rho_\infty U^2}{2\pi} \frac{1}{Ut} \int_0^L [A_b'(X)]^2 dX . \tag{2.41}$$

More precisely, this limit corresponds to $a_\infty t / R \to \infty$; i.e., $R \ll a_\infty t \ll L$ and pressure waves propagate at a distance, which is much larger than the body radius and much smaller than the body length.

The expression (2.41) can be derived by considering (1.11) at $\varepsilon = a_\infty t$

$$-4\pi\phi = -4\pi\phi_{II}(x,r,t) = \int_{x-a_\infty t}^{x+a_\infty t} \frac{Q\left(\xi, t - \frac{\sqrt{(x-\xi)^2 + r^2}}{a_\infty}\right)}{\sqrt{(x-\xi)^2 + r^2}} d\xi . \tag{2.42}$$

Using (1.16) we obtain for $a_\infty t \to 0$ and $r/(a_\infty t) \to 0$

$$-4\pi\phi = 2Q(x,t)\log\frac{2a_\infty t}{r} + O\left(\varepsilon, \frac{r^2}{(a_\infty t)^2}\right). \tag{2.43}$$

Using (1.29) we write (2.43) as

$$\phi = \frac{U}{2\pi} A_b'(X) \log\frac{r}{2a_\infty t} . \tag{2.44}$$

Then

$$\frac{\partial\phi}{\partial r} = \frac{U}{2\pi} A_b'(X)\frac{1}{r}, \tag{2.45}$$

$$\frac{\partial\phi}{\partial t} = \frac{U^2}{2\pi} A_b''(X)\left(\log r - \log 2a_\infty t\right) - \frac{U}{2\pi}\frac{A_b'(X)}{t}. \tag{2.46}$$

Using (2.2) we obtain the wall pressure

$$p_w = -\rho_\infty \left[\frac{\partial \phi}{\partial t} + \frac{1}{2}\left(\frac{\partial \phi}{\partial r}\right)^2 \right]_{r=r_b(X)} =$$

$$\frac{\rho_\infty U^2}{2\pi}\left[-\frac{1}{4\pi}\frac{A_b'^2(X)}{r_b^2(X)} - A_b''(X)\log r_b(X) - A_b''(X)\log 2a_\infty t + \frac{A_b'(X)}{Ut} \right]$$

(2.47)

Then the wave drag is expressed as

$$D(t) = \int_0^L p_w(X,t)A_b'(X)dX =$$

$$= \frac{\rho_\infty U^2}{2\pi}\int_0^L \left[-\frac{1}{4\pi}\frac{A_b'^2(X)}{r_b^2(X)} - A_b''(X)\log r_b(X) - A_b''(X)\log 2a_\infty t + \frac{A_b'(X)}{Ut} \right]A_b'(X)dX$$

The first two terms give

$$-\int_0^L \left[A_b'(X)A_b''(X)\log r_b(X) + \frac{r_b'(X)}{2r_b(X)}[A_b'(X)]^2 \right]dX = -\int_0^L \frac{d}{dX}\left[\frac{1}{2}A_b'^2(X)\log r_b(X) \right]dX = 0$$

The third term is zero since $A_b'(0) = A_b'(L) = 0$, and the forth term gives the expression

$$D(t) = \frac{\rho_\infty U^2}{2\pi}\frac{1}{Ut}\int_0^L A_b'^2(X)dX .$$

(2.48)

that coincide with (2.41).

According to (2.48) the wave drag tends to infinity as $t \to 0$. To resolve this singularity we should consider a much shorter time interval in which $a_\infty t = O(R)$. The expression (1.16) gives

$$-4\pi\phi = \int_{x-a_\infty t}^{x+a_\infty t} \frac{Q\left(\xi, t - \frac{\sqrt{(x-\xi)^2 + r^2}}{a_\infty}\right)}{\sqrt{(x-\xi)^2 + r^2}}d\xi = 2Q(x,t)\log\left(\frac{a_\infty t}{r} + \sqrt{\left(\frac{a_\infty t}{r}\right)^2 + 1}\right) + O(a_\infty t).$$ (2.49)

It is immediately seen that for very short time, $a_\infty t / r \to 0$, (2.49) gives

$$\phi = -\frac{Q(x,t)}{2\pi}\frac{a_\infty t}{r} = -\frac{U}{2\pi}A_b'(X)\frac{a_\infty t}{r} .$$

(2.50)

The wall pressure is

$$p_w = -\rho_\infty \left[\frac{\partial \phi}{\partial t} + \frac{1}{2}\left(\frac{\partial \phi}{\partial r}\right)^2 \right]_{r=r_b(X)} = \frac{\rho_\infty Ua_\infty}{2\pi}\left[\frac{A_b'(X)}{r_b(X)} + ... \right]$$

Then the wave drag at $t = 0$ is

$$D(0) = \frac{\rho_\infty Ua_\infty}{2\pi}\int_0^L \frac{A_b'^2(X)}{r_b(X)}dX = \frac{\rho_\infty U^2}{2}\frac{2}{M}\int_0^L r_b'(X)A_b'(X)dX = \rho_\infty U^2 L^2 O(\delta^3),$$

(2.51)

xvi

where $\delta = r_{b,\max} / L$ is the body thickness ratio.

Note that the steady-flight drag

$$D_A = -\frac{\rho_\infty U^2}{2\pi} \int_0^L \left[A_b''(X) \int_0^X \log(X-\sigma) A_b''(\sigma) d\sigma \right] dX = \rho_\infty U^2 L^2 O(\delta^4) . \tag{2.52}$$

For brevity we write (2.49) in the form

$$\phi = -\frac{1}{2\pi} Q(x,t) \log F(r,t) = -\frac{U}{2\pi} A_b'(X) \log F(r,t) , \tag{2.53}$$

where

$$F(r,t) = \frac{a_\infty t}{r} + \sqrt{\left(\frac{a_\infty t}{r}\right)^2 + 1} , \tag{2.54}$$

$$\frac{\partial F}{\partial t} = \frac{a_\infty}{r}\left(1 + \frac{\frac{a_\infty t}{r}}{\sqrt{\left(\frac{a_\infty t}{r}\right)^2 + 1}}\right) = \frac{\frac{a_\infty}{r}}{\sqrt{\left(\frac{a_\infty t}{r}\right)^2 + 1}} F = \frac{a_\infty}{\sqrt{(a_\infty t)^2 + r^2}} F , \tag{2.55}$$

$$\frac{\partial F}{\partial r} = -\frac{a_\infty t}{r^2}\left(1 + \frac{\frac{a_\infty t}{r}}{\sqrt{\left(\frac{a_\infty t}{r}\right)^2 + 1}}\right) = -\frac{\frac{a_\infty t}{r}}{\sqrt{(a_\infty t)^2 + r^2}} F , \tag{2.56}$$

$$\frac{\partial \phi}{\partial t} = -\frac{U^2}{2\pi} A_b''(X) \log F - \frac{U}{2\pi} \frac{A_b'(X)}{F} \frac{\partial F}{\partial t} = -\frac{U^2}{2\pi} A_b''(X) \log F - \frac{U A_b'(X)}{2\pi} \frac{a_\infty}{\sqrt{(a_\infty t)^2 + r^2}} , \tag{2.57}$$

$$\frac{\partial \phi}{\partial r} = -\frac{U}{2\pi} A_b'(X) \frac{1}{F} \frac{\partial F}{\partial r} = \frac{U}{2\pi} A_b'(X) \frac{\frac{a_\infty t}{r}}{\sqrt{(a_\infty t)^2 + r^2}} . \tag{2.58}$$

Then the wall pressure is

$$p_w(X,t) = -\rho_\infty \left[\frac{\partial \phi}{\partial t} + \frac{1}{2}\left(\frac{\partial \phi}{\partial r}\right)^2 \right]_{r=r_b(X)} = \frac{\rho_\infty U^2}{2\pi}\left[A_b''(X) \log F(r_b(X),t) + \frac{A_b'(X)}{M} \frac{1}{\sqrt{(a_\infty t)^2 + r_b^2(X)}} \right] -$$

$$-\frac{\rho_\infty U^2}{2\pi}\left[\frac{1}{4\pi} \frac{\left(A_b'(X)\frac{a_\infty t}{r_b(X)}\right)^2}{(a_\infty t)^2 + r_b^2(X)} \right]$$

and the wave drag (for short time intervals) is expressed as

$$D_0(t) = \frac{\rho_\infty U^2}{2} \int_0^L A_b'(X) G(X,t) dX \tag{2.59}$$

$$G(X,t) = \frac{1}{\pi}\left[A_b''(X) \log F(r_b(X),t) + \frac{A_b'(X)}{M} \frac{1}{\sqrt{(a_\infty t)^2 + r_b^2(X)}} \right] -$$
$$- \frac{(r_b'(X) a_\infty t)^2}{(a_\infty t)^2 + r_b^2(X)} \tag{2.60}$$

The expressions (2.59) and (2.60) are convenient for numerical integration.

Combining (2.59) with (2.40) and subtracting their common part, we obtain a composite formula for $0 < t < L/(U + a_\infty)$

$$D(t) = D_A + D_{AB}(t) + D_{BC}(t) + D_0(t) - \frac{\rho_\infty U^2}{2\pi} \frac{1}{Ut} \int_0^L \left[A_b'(X) \right]^2 dX , \tag{2.61}$$

where the last term represent subtraction of the common part.

2.7 Summary of analysis

Summarizing the foregoing results, we outline formulas for the wave drag:

For $t > L/(U - a_\infty)$

$$D_A = -\frac{\rho_\infty U^2}{2\pi} \int_0^L \left[A_b''(X) \int_0^X \log(X-\sigma) A_b''(\sigma) d\sigma \right] dX . \tag{2.62}$$

For $L/(U + a_\infty) < t < L/(U - a_\infty)$

$$D(t) = D_A + D_{AB}(t) \tag{2.63}$$

$$D_{AB}(t) = \frac{\rho_\infty U^2}{4\pi} \frac{1}{Ut} \int_{(U-a_\infty)t}^L A_b'(X - (U - a_\infty)t) A_b'(X) dX -$$
$$- \frac{\rho_\infty U^2}{4\pi} \int_{(U-a_\infty)t}^L \left[\int_0^{X-(U-a_\infty)t} \frac{A_b''(\sigma)}{X-\sigma} d\sigma \right] A_b'(X) dX \tag{2.64}$$

For $0 < t < L/(U + a_\infty)$

$$D(t) = D_A + D_{AB}(t) + D_{BC}(t) + D_0(t) - \frac{\rho_\infty U^2}{2\pi} \frac{1}{Ut} \int_0^L \left[A_b'(X) \right]^2 dX \tag{2.65}$$

$$D_{BC}(t) = \frac{\rho_\infty U^2}{4\pi} \frac{1}{Ut} \int_{(U+a_\infty)t}^{L} A_b'(X-(U+a_\infty)t)A_b'(X)dX -$$

$$-\frac{\rho_\infty U^2}{4\pi} \int_{(U+a_\infty)t}^{L} \left[\int_0^{X-(U+a_\infty)t} \frac{A_b''(\sigma)}{X-\sigma}d\sigma \right] A_b'(X)dX \tag{2.66}$$

$$D_0(t) = \frac{\rho_\infty U^2}{2} \int_0^L A_b'(X)G(X,t)dX \tag{2.67}$$

$$G(X,t) = \frac{1}{\pi}\left[A_b''(X)\log F(r_b(X),t) + \frac{A_b'(X)}{M}\frac{1}{\sqrt{(a_\infty t)^2+r_b^2(X)}} \right] -$$

$$-\frac{(r_b'(X)a_\infty t)^2}{(a_\infty t)^2+r_b^2(X)} \tag{2.68}$$

For $t=0$

$$D(0) = \frac{\rho_\infty U^2}{2}\frac{2}{M}\int_0^L r_b'(X)A_b'(X)dX. \tag{2.69}$$

These relations are used for calculations discussed hereafter.

3. Numerical examples

The FORTRAN code "Wave Drag" was developed to calculate the wave-drag time history, $D(t)$, using the relations (2.62)-(2.68). Numerical examples were generated for the body shape

$$r_b(X) = r_{max}\sin(\pi X/L).$$

In the dimensionless variables $\bar{X} = X/L$ and $\bar{r}_b = r_b/L$, this shape is expressed as

$$\bar{r}_b = \delta\sin(\pi\bar{X}). \tag{2.70}$$

Calculations were carried out for $\delta = 0.05$. The body shape characteristics are shown in Figure A4.

Figure A5 shows the drag coefficient $C_D(T) = \dfrac{D(T)}{A_{max}\rho_\infty U^2/2}$ for the case of Mach number $M = U/a_\infty = 2$, where $T = ta_\infty/L$ is nondimensional time and $A_{max} = \pi r_{b,max}^2 = \pi\delta^2 L^2$ is maximum cross-sectional area. The characteristic times $T_0 = \delta$ ($t_0 = r_{b,max}/a_\infty$), $T_A = 1/(M-1)$ ($t_A = L/(U+a_\infty)$) and $T_B = 1/(M+1)$ ($t_B = L/(U+a_\infty)$) are marked by arrows. The circle shows $C_D(0)$ calculated using (2.69). For $T > T_A$, the transient process is over and the wave drag coefficient is constant. Note that this coefficient does not depend on Mach number. In accord

with (2.62) it is a function of the body shape only. The initial wave-drag coefficient $C_D(0)$ is significantly higher than C_D relevant to steady flight. The drag quickly decreases in the time interval $T = O(\delta)$ and then relatively slow approaches the steady state level.
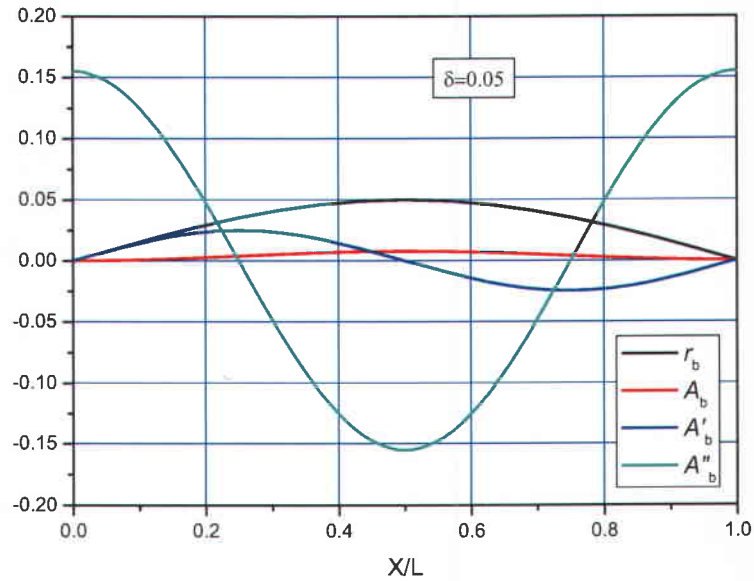
Figure A4 Characteristics of the body shape (2.70), $\delta = 0.05$.
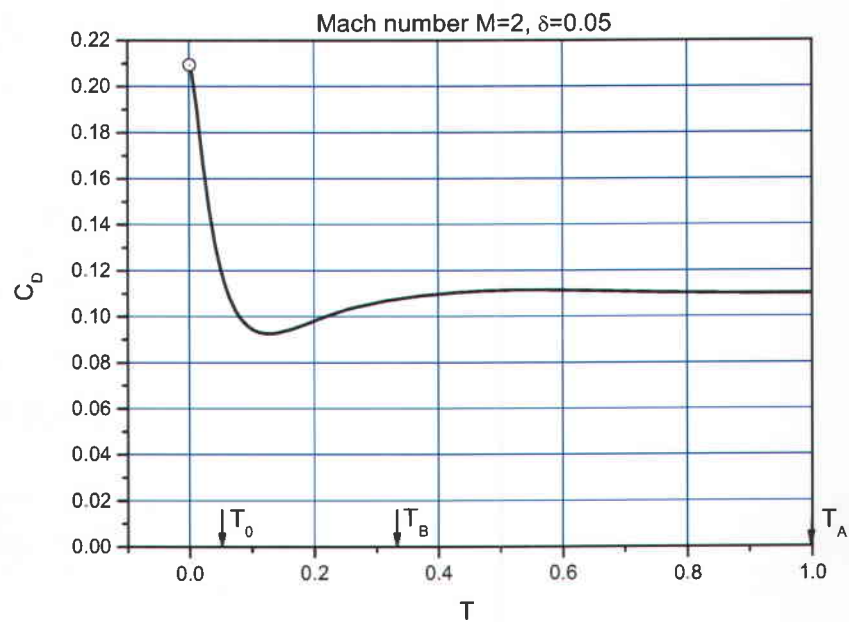
Figure A5 Wave drag coefficient $C_D(T)$ for $M = 2$, $\delta = 0.05$.

Figure A6 shows $C_D(T)$ for different Mach numbers. As expected, the transient time increases and tends to infinity as the Mach number decreases and approaches $M = 1$ (transonic case). Note that the transonic case needs special treatments, since the linear acoustic theory is not valid in the vicinity of $M = 1$ even for slender bodies.
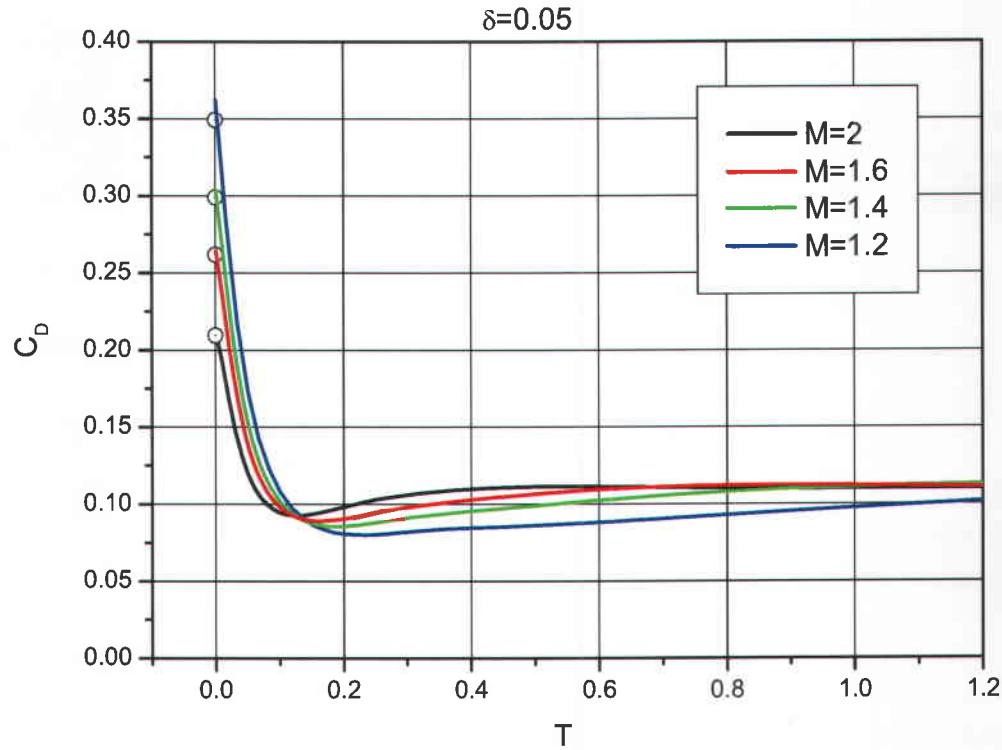
Figure A6 Wave drag coefficients $C_D(T)$ for various Mach numbers, $\delta = 0.05$.

4. Comparison with Euler CFD solution

Numerical calculations of an axisymmetric inviscid flow over a slender body of revolution were carried out for the free-stream parameters:

- Mach number $M_\infty = 2$
- Static pressure $p_\infty = 383410 \, \text{Pa}$
- Temperature $T_\infty = 277 \, \text{K}$
- Density $\rho_\infty = 4.8222 \, \text{kg/m}^3$
- Velocity $U_\infty = 667.03 \, \text{m/s}$

The body shape is given by (2.70) with the parameters:

- Body length $L = 1 \, \text{m}$
- Thickness ratio $\delta = 0.01$

Near the nosetip $\overline{X} \to 0$, the body radius is $r_b \approx \delta\pi\overline{X}$ that gives the nose half-angle $\alpha \approx \delta\pi = \dfrac{\pi}{100} = 1.8°$. Note that the Mach wave angle is $\gamma = \arcsin\left(M_\infty^{-1}\right) = 30°$.
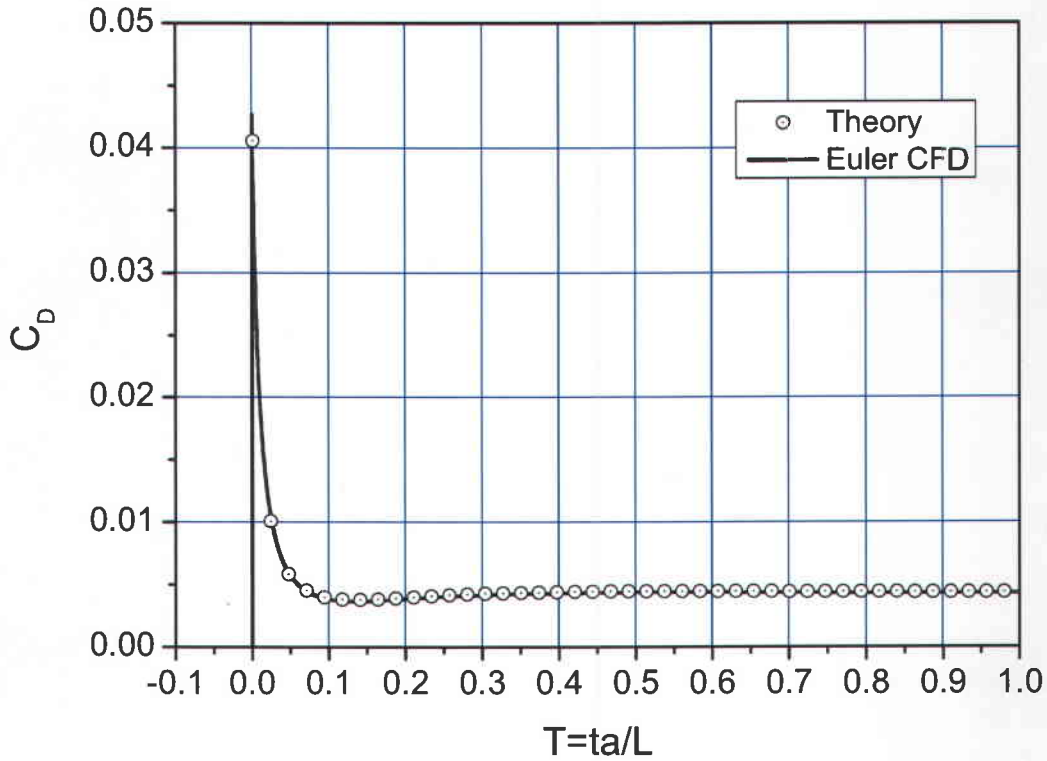
Figure A7 The drag coefficient C_D as a function of time $T = ta_\infty / L$, solid line – CFD, symbols – theoretical solution summarized in Section 2.7.

The computational grid contains approximately 10^5 cells: ≈ 300 grid points along the body surface and ≈ 300 grid points in the direction normal to the body surface.

The drag coefficient versus time is shown in Figures A7 and A8 (black lines) for relatively large and short initial time intervals, respectively. The wave drag almost instantaneously reaches its maximum, decreases with time to the minimum $C_D \approx 3.65\times10^{-3}$ at $T \approx 0.13$, and then tends to the steady-state level $C_D \approx 4.4\times10^{-3}$. The CFD solution (black line) agrees well with the theoretical solution summarized in Section 2.7.

Instantaneous pressure fields at various time moments (CFD solution) are shown in Figure A9. In accord with linear acoustic theory, the body-induced pressure waves propagate along characteristics and, finally, form a steady-state pressure field around the body moving with constant Mach number. For this steady field, distributions of axial and radial velocity, temperature and Mach number are shown in Figures A10-A13.
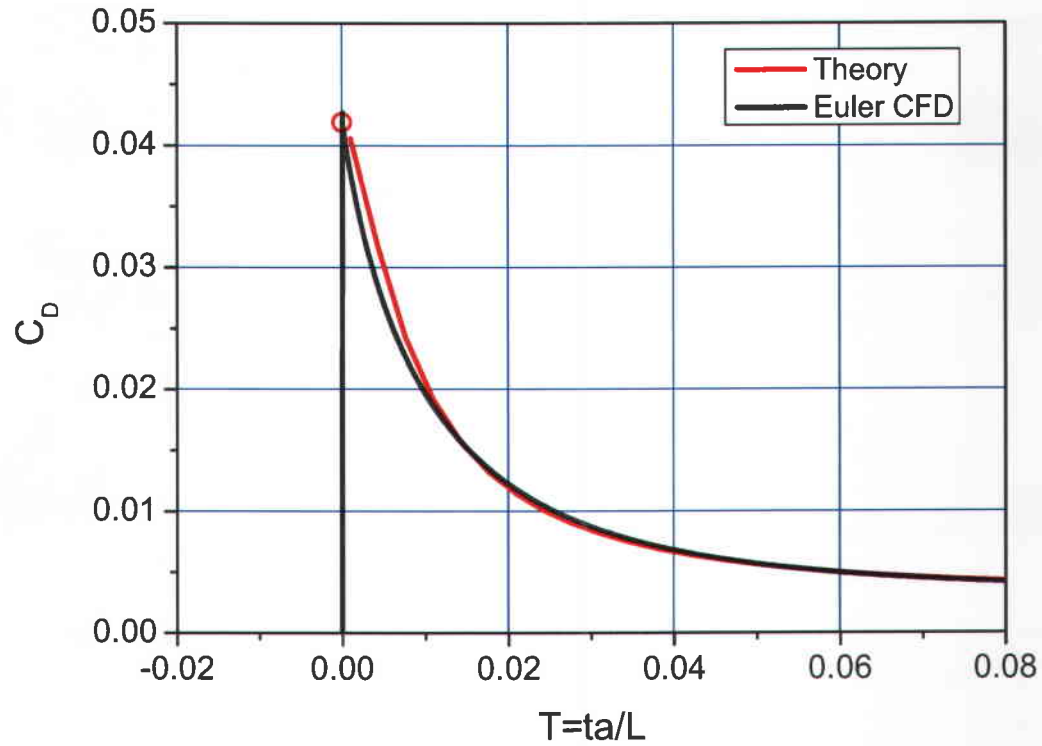
Figure A8 The drag coefficient C_D as a function of $T = ta_\infty / L$ for the initial time interval, black line – CFD, red line – theoretical solution summarized in Section 2.7, red circle – $C_D(0)$ calculated using (2.69).

$t = 1.5 \times 10^{-6}$ sec
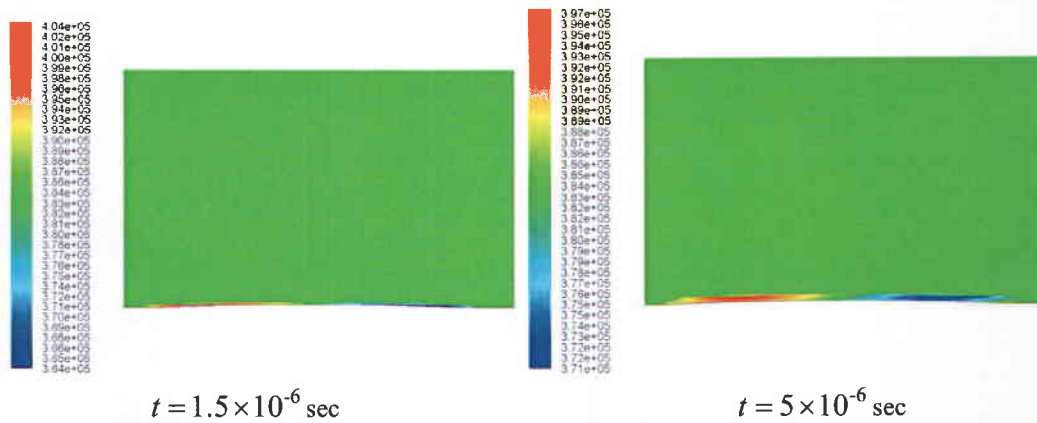
$t = 5 \times 10^{-6}$ sec

$t = 6 \times 10^{-6}$ sec.

$t = 8 \times 10^{-6}$ sec.
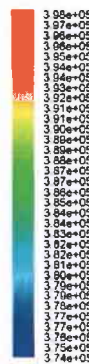
$t = 10 \times 10^{-6}$ sec.

$t = 12 \times 10^{-6}$ sec.
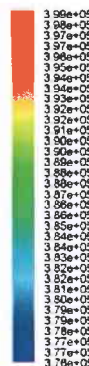
$t = 14 \times 10^{-6}$ sec

$t = 16 \times 10^{-6}$ sec

$t = 18 \times 10^{-6}$ sec

$t = 20 \times 10^{-6}$ sec

$t = 30 \times 10^{-6} \text{ sec}$

$t = 40 \times 10^{-6} \text{ sec}$

$t = 50 \times 10^{-6} \text{ sec}$

$t = 60 \times 10^{-6} \text{ sec}$

$t = 70 \times 10^{-6} \text{ sec}$

$t = 80 \times 10^{-6} \text{ sec}$

$t = 90 \times 10^{-6} \text{ sec}$

$t = 100 \times 10^{-6} \text{ sec}$

$t = 110 \times 10^{-6}$ sec $\qquad\qquad\qquad$ $t = 120 \times 10^{-6}$ sec

$t = 130 \times 10^{-6}$ sec $\qquad\qquad\qquad$ $t = 140 \times 10^{-6}$ sec

$t = 150 \times 10^{-6}$ sec. $\qquad\qquad\qquad$ $t = 160 \times 10^{-6}$ sec
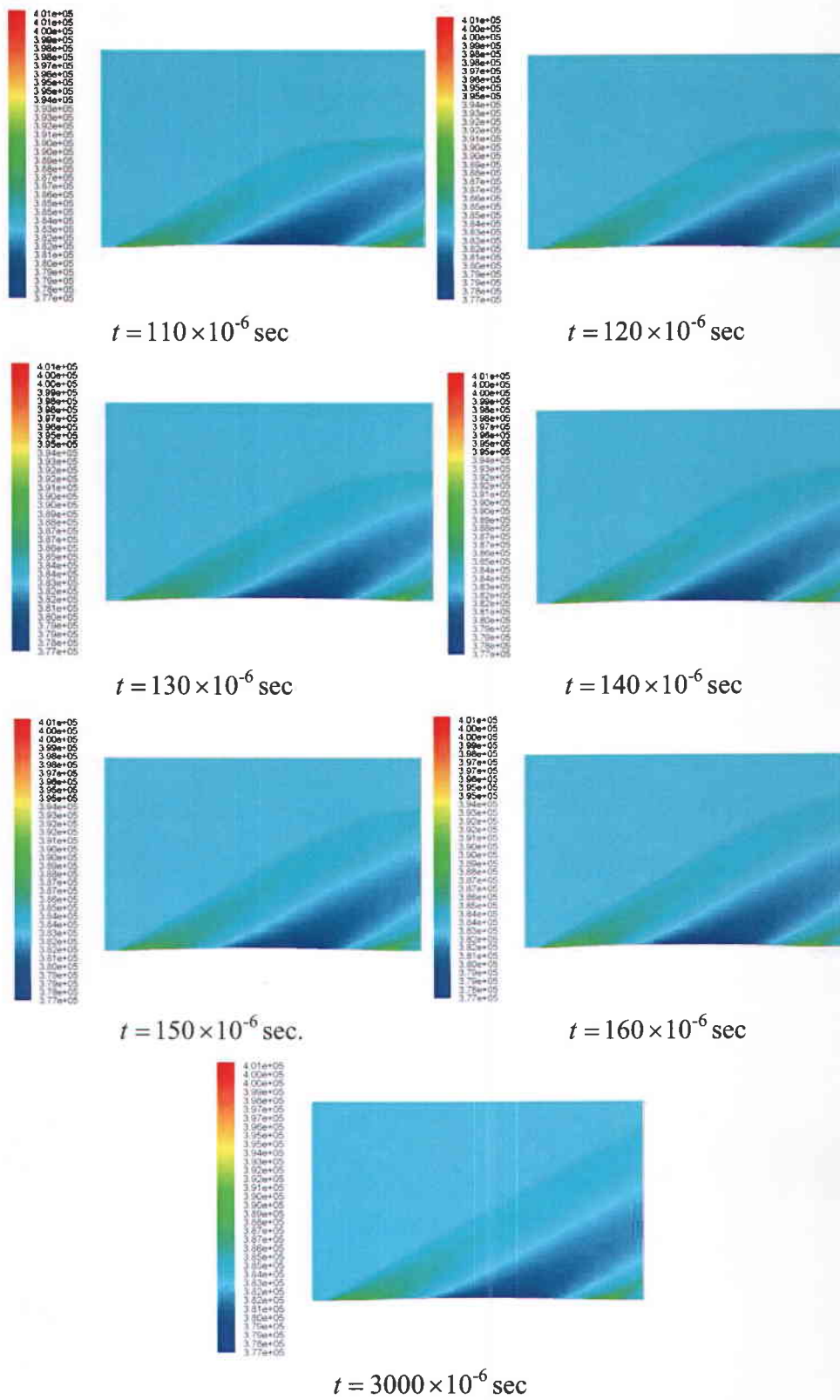
$t = 3000 \times 10^{-6}$ sec

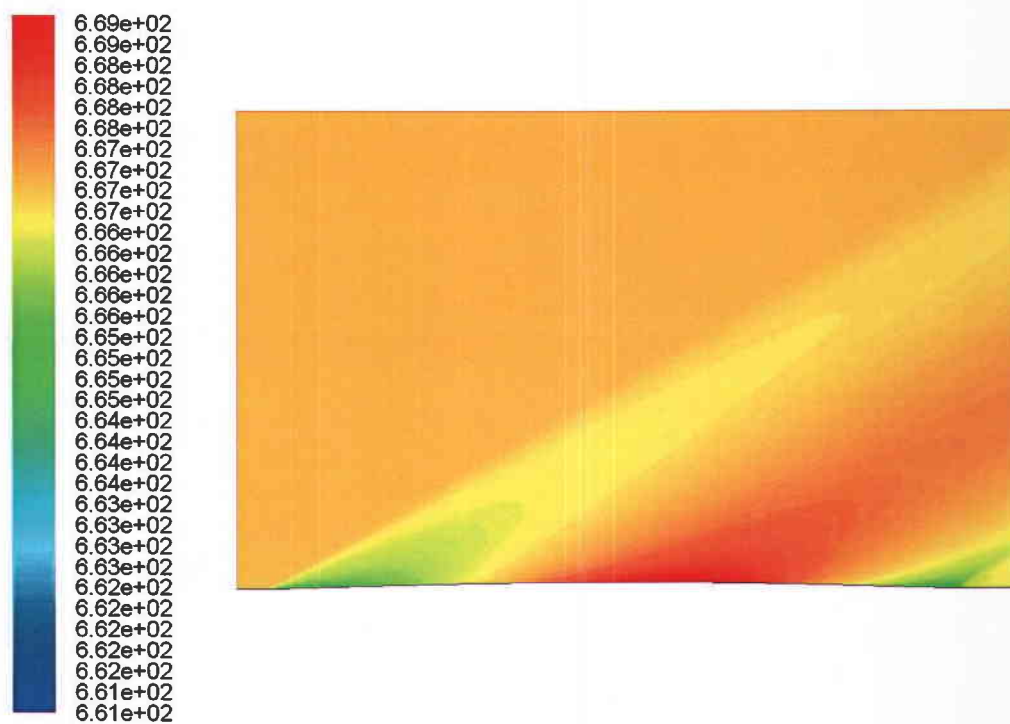**Figure A9** Evolution of static pressure field.

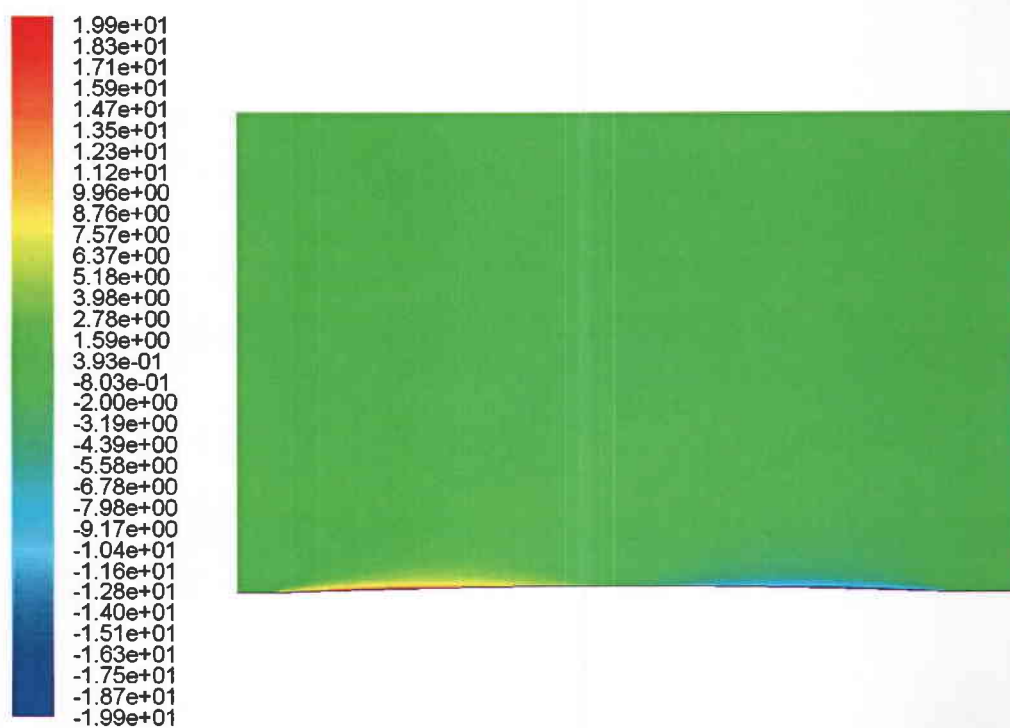**Figure A10** Axial velocity at $t = 3000 \times 10^{-6}$ sec.
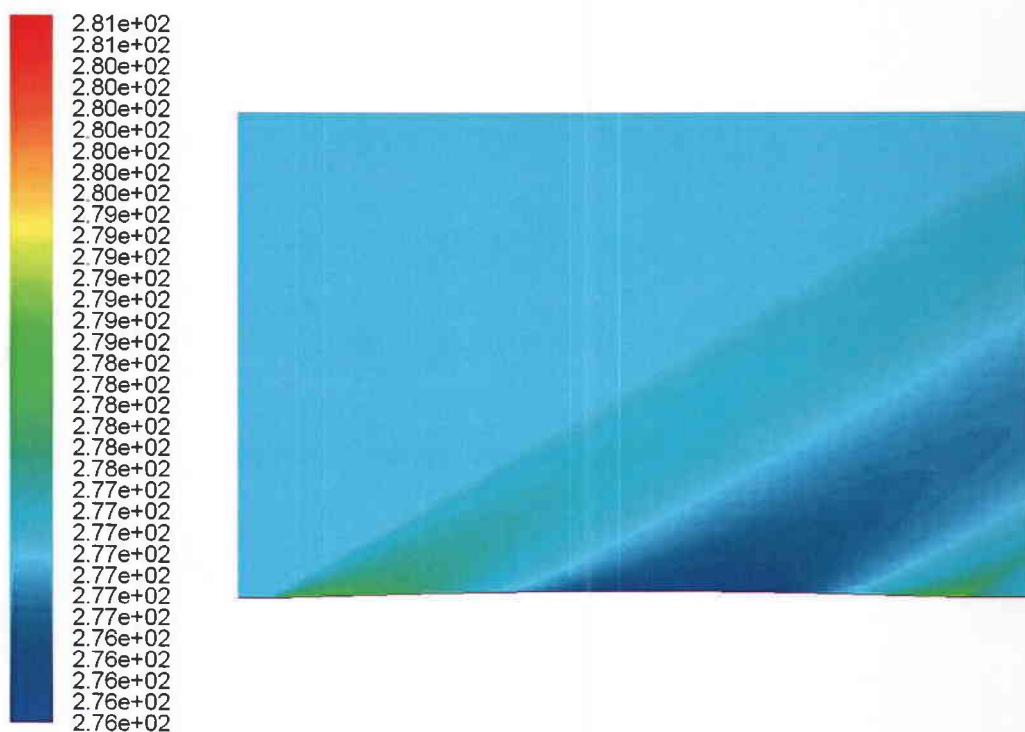

Figure A11 Radial velocity at $t = 3000 \times 10^{-6}$ sec.

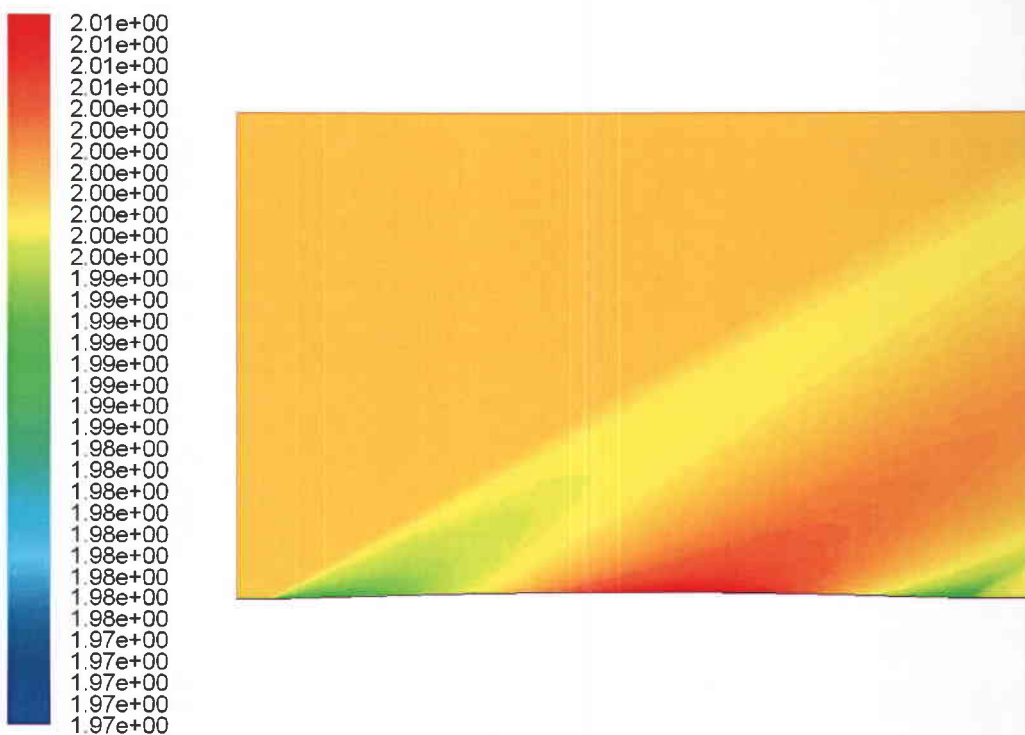**Figure A12** Temperature at $t = 3000 \times 10^{-6}$ sec.

Figure A13 Mach number at $t = 3000 \times 10^{-6}$ sec.

5. Conclusions

1. Mathematical modeling of unsteady effects associated with acceleration of the body center of gravity has been carried out. Namely, we have conducted theoretical analysis of the wave drag generated by a non-lifting body of revolution during its instantaneous supersonic start. The analysis is based on linear acoustic theory and asymptotic techniques.

2. Typical phases of the transient process were identified. Analytical expressions of the flow potential were derived for each phase. These expressions were used to obtained the pressure distribution on the body surface and calculate the wave drag.

3. It was shown that in the initial time interval $R \ll a_\infty t \ll L$, the wave-drag solution is singular. Asymptotic analysis of this initial phase of transient process allowed us to resolve the singularity, obtain an analytical expression for the initial wave drag $D(t=0)$ and build up a composite solution convenient for computations.

4. The aforementioned theoretical results were incorporated into a FORTRAN code providing quick calculations of the wave drag time history. Numerical examples were generated for a slender body of half-sine shape with thickness ratio $\delta = 0.05$ for different Mach numbers (M=1.2, 1.4, 1.6 and 2) of instantaneous body start. It was shown that the initial wave-drag coefficient $C_D(t=0)$ is significantly larger than C_D relevant to steady flight. The wave drag quickly decreases in the time interval $t \sim \delta L / a_\infty$ and then relatively slow approaches the steady-state level. The transient time increases and tends to infinity as the Mach number decreases and approaches $M=1$ of transonic flow.

5. The transient process was also simulated numerically by solving 3-D Euler equations for Mach=2 start of the aforementioned body with $\delta = 0.01$. It was shown that the theoretical wave drag $D(t)$ is in excellent agreement with that predicted by CFD in all phases of the transient process.

These results provide a good launching pad for theoretical modeling of unsteady body motions including the coupling between body dynamics and aerodynamics.

References

1. Cole, J.D., and Cook, L.P., *Transonic Aerodymamics*. Elsevier Science Publishers B.V., 1986.

2. Cole, J.D., "Note on Nonstationary Slender-Body Theory," *J. Aeronautical Sciences*, November 1953, pp. 798-799.

3. Crow, S.C., and Bergmeier, G.G., "Active Sonic Boom Control," *J. Fluid Mech.*, Vol. 325, 1996, pp. 1-28.

4. von Karman, Th., and Moore, N.B., "Resistance of Slender Bodies Moving with Supersonic Velocities with Special Reference to Projectiles," Trans. Am. Soc. Mech. Engrs., 54, 1932, pp. 303-310.

5. Witham, G.B., Linear and Nonlinear Waves. John Wiley & Sons, 1999.